Full top quark mass dependence in Higgs boson pair production at NLO

S. Borowka,[a] **N. Greiner,**[a] **G. Heinrich,**[b] **S.P. Jones,**[b] **M. Kerner,**[b] **J. Schlenk**[b] **and T. Zirke**[b]

[a]*Institute for Physics, Universität Zürich,*
Winterthurerstr.190, 8057 Zürich,Switzerland

[b]*Max-Planck-Institute for Physics,*
Föhringer Ring 6, 80805 München, Germany

E-mail: sophia.borowka@cern.ch, greiner@physik.uzh.ch, gudrun@mpp.mpg.de, sjones@mpp.mpg.de, kerner@mpp.mpg.de, johannes.k.schlenk@durham.ac.uk, zirke@mpp.mpg.de

ABSTRACT: We study the effects of the exact top quark mass-dependent two-loop corrections to Higgs boson pair production by gluon fusion at the LHC and at a 100 TeV hadron collider. We perform a detailed comparison of the full next-to-leading order result to various approximations at the level of differential distributions and also analyse non-standard Higgs self-coupling scenarios. We find that the different next-to-leading order approximations differ from the full result by up to 50 percent in relevant differential distributions. This clearly stresses the importance of the full NLO result.

Contents

1 Introduction

After the discovery of a boson [1, 2] whose characteristics have so far been consistent with the Standard Model Higgs boson, it is a primary goal of the LHC and future colliders to further scrutinize its properties. In particular, the form of the Higgs potential needs to be reconstructed by experimental measurements, in order to confirm the mechanism of electroweak symmetry breaking postulated by the Standard Model. One of the parameters entering the Higgs potential, the mass of the Higgs boson, already has been measured to an impressive precision [3]. The other parameter, the Higgs boson self-coupling, is more difficult to constrain, as it requires the production of at least two Higgs bosons. The cross sections for Higgs boson pair production at the LHC are about three orders of magnitude smaller than the ones for single Higgs production. The dominant production channel is the gluon fusion channel, as for single Higgs boson production at the LHC.

In the gluon fusion channel, there are two categories of contributions to di-Higgs production: either a virtual Higgs boson, produced by the same mechanism as in single Higgs production, is decaying into a Higgs boson pair, involving the self-coupling λ_{hhh}, or the two Higgs bosons are both directly radiated from a heavy quark. At leading order (LO),

these two mechanisms can be attributed to "triangle" and "box" contributions, respectively. However, at NLO, i.e. at the level of two-loop diagrams, the diagram topologies are more complicated, such that the association of "triangle diagrams" to diagrams containing the self-coupling λ_{hhh} becomes invalid.

The Higgs boson pair production cross section is additionally suppressed by the fact that there is destructive interference between contributions containing the Higgs boson self-coupling and the ones containing only Yukawa couplings to heavy quarks, and that for larger values of $\sqrt{\hat{s}}$, the contributions with an s-channel virtual Higgs boson propagator are strongly suppressed.

Therefore, narrowing the window of possible values for the triple-Higgs coupling experimentally will have to wait until the high-luminosity run of the LHC [4–6], if Standard Model rates are assumed. However, the Higgs boson pair production rate could be modified by physics beyond the Standard Model (BSM), and hence it is important to be able to distinguish BSM effects from Standard Model higher order corrections. In this paper we will study the effects of a modified Higgs boson self-coupling and show that the Higgs boson invariant mass distribution is quite sensitive to changes in λ_{hhh}, as such changes modify the interference pattern.

Both ATLAS and CMS have published measurements of Higgs boson pair production in the decay channels $\gamma\gamma b\bar{b}$ [7–10], $b\bar{b}b\bar{b}$ [9, 11–14], $\gamma\gamma WW^*$, $b\bar{b}WW^*$, $\tau^+\tau^- b\bar{b}$ [9, 15–21].

Phenomenological studies about Higgs boson pair production and the feasibility of Higgs boson self-coupling measurements can be found e.g. in refs. [22–50].

The leading order (one-loop) calculation of Higgs boson pair production in gluon fusion has been performed in refs. [51–53]. NLO corrections were calculated in the $m_t \to \infty$ limit, where the top quark degrees of freedom are integrated out, leading to point-like effective couplings of gluons to Higgs bosons ("Higgs Effective Field Theory", HEFT).

Top quark mass effects have been included in various approximations. Calculating the NLO corrections within the heavy top limit and then rescaling the result differentially by a factor $B_{\rm FT}/B_{\rm HEFT}$, where $B_{\rm FT}$ denotes the leading order matrix element squared in the full theory, is denoted "Born-improved HEFT" approximation. This calculation [54], implemented in the program Hpair, led to a K-factor of about two. In ref. [55], another approximation, called "FT$_{\rm approx}$", was introduced, which contains the full top quark mass dependence in the real radiation, while the virtual part is calculated in the HEFT approximation and rescaled by the re-weighting factor $B_{\rm FT}/B_{\rm HEFT}$. The "FT$'_{\rm approx}$" result [55] in addition uses partial NLO results for the virtual part, i.e. it employs the exact results where they are known from single Higgs production. The "FT$_{\rm approx}$" calculation leads to a cross section which is about 10% smaller than the Born-improved NLO HEFT cross section. Using the "FT$'_{\rm approx}$" procedure, the reduction is about 9% with respect to the Born-improved NLO HEFT result. It was also found that top width effects can reach up to -4% above the $t\bar{t}$ threshold [55]. At LO, a finite top width reduces the total cross section at $\sqrt{s} = 14\,{\rm TeV}$ by about 2%. In our calculation we do not include a finite top width.

In addition, the HEFT results at NLO and NNLO have been improved by an expansion in $1/m_t^{2\rho}$ in refs. [56–59], with $\rho^{\rm max} = 6$ at NLO, and $\rho^{\rm max} = 2$ for the soft-virtual part at NNLO [58]. In the latter reference it is also demonstrated that the sign of the finite top
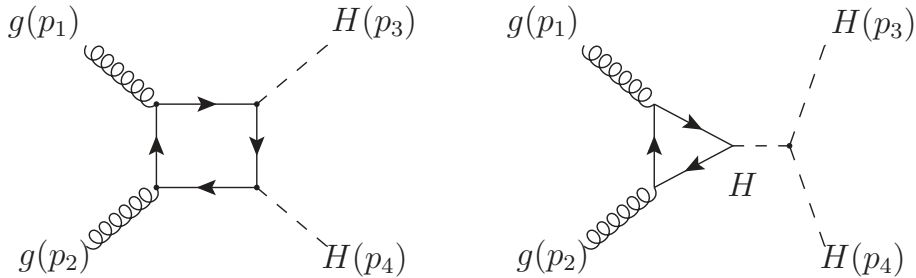
Figure 1. Diagrams contributing to the process $gg \to hh$ at leading order.

mass corrections, amounting to about $\pm 10\%$, depends on whether the re-weighting factor is applied at differential level, i.e. before the integration over the partonic centre of mass energy, or at total cross section level.

The NNLO QCD corrections in the heavy top limit have been performed in refs. [57, 60, 61], and they have been supplemented by an expansion in $1/m_t^2$ in ref. [58] and by resummation at NLO+NNLL in ref. [62]. The most precise results within the infinite top mass approximation are NNLO+NNLL resummed results, calculated in ref. [63], leading to K-factors of about 1.2 relative to the Born-improved HEFT result. Very recently, fully differential NNLO results in the HEFT approximation have become available [64].

As the different approximations partly led to corrections with opposite sign, there was a rather large uncertainty associated with the unknown effect of the exact top quark mass dependence at NLO, which was estimated to be of the order of 10% at $\sqrt{s} = 14 \, \text{TeV}$.

The full NLO calculation which became available recently [65], revealed a 14% reduction of the total cross section compared to the Born improved HEFT at $\sqrt{s} = 14 \, \text{TeV}$ and a 24% reduction at $\sqrt{s} = 100 \, \text{TeV}$.

At differential distribution level, we found that the deviation from the Born-improved HEFT approximation can be as large as 50% in the tails of distributions like the Higgs boson pair invariant mass or Higgs boson transverse momentum distributions.

This paper is structured as follows. In section 2 we give details of the calculation, in particular about the calculation of the two-loop amplitude and about the $1/m_t$ expansion which we also performed. In section 3 we discuss our phenomenological results. We study various distributions at $\sqrt{s} = 14 \, \text{TeV}$ and $\sqrt{s} = 100 \, \text{TeV}$, comparing the full NLO result to different approximations. We also analyze the effects of non-Standard Model values of the triple Higgs coupling.

2 Details of the calculation

2.1 Amplitude structure

The leading order diagrams contributing to the process $gg \to hh$ are shown in figure 1. As the cross section does not have a tree level contribution, the virtual contribution at next-to-leading order involves two-loop diagrams, and the NLO real radiation part involves one-loop diagrams up to pentagons.

The amplitude for the process $g(p_1, \mu) + g(p_2, \nu) \to h(p_3) + h(p_4)$ can be decomposed into form factors as

$$\mathcal{M}_{ab} = \delta_{ab}\, \epsilon^\mu(p_1, n_1) \epsilon^\nu(p_2, n_2)\, \mathcal{M}_{\mu\nu} \tag{2.1}$$

$$\mathcal{M}^{\mu\nu} = \frac{\alpha_s}{8\pi v^2} \left\{ F_1(\hat{s}, \hat{t}, m_h^2, m_t^2, D)\, T_1^{\mu\nu} + F_2(\hat{s}, \hat{t}, m_h^2, m_t^2, D)\, T_2^{\mu\nu} \right\} ,$$

where n_1, n_2 are arbitrary reference momenta for the two gluon polarization vectors $\epsilon^\mu, \epsilon^\nu$. Colour indices are denoted by a, b and

$$\hat{s} = (p_1 + p_2)^2, \quad \hat{t} = (p_1 - p_3)^2, \quad \hat{u} = (p_2 - p_3)^2 . \tag{2.2}$$

The decomposition into tensors carrying the Lorentz structure is not unique. It is however convenient to define the form factors such that [52]

$$\mathcal{M}^{++} = \mathcal{M}^{--} = -\frac{\alpha_s}{8\pi v^2}\, F_1 \tag{2.3}$$

$$\mathcal{M}^{+-} = \mathcal{M}^{-+} = -\frac{\alpha_s}{8\pi v^2}\, F_2 ,$$

which is fulfilled with the following definitions

$$T_1^{\mu\nu} = g^{\mu\nu} - \frac{p_1^\nu p_2^\mu}{p_1 \cdot p_2} , \tag{2.4}$$

$$T_2^{\mu\nu} = g^{\mu\nu} + \frac{1}{p_T^2 (p_1 \cdot p_2)} \left\{ m_h^2\, p_1^\nu p_2^\mu - 2 (p_1 \cdot p_3)\, p_3^\nu p_2^\mu \right.$$
$$\left. - 2 (p_2 \cdot p_3)\, p_3^\mu p_1^\nu + 2 (p_1 \cdot p_2)\, p_3^\nu p_3^\mu \right\}$$

where $\quad p_T^2 = (\hat{u}\,\hat{t} - m_h^4)/\hat{s} , \; T_1 \cdot T_2 = D - 4 , \; T_1 \cdot T_1 = T_2 \cdot T_2 = D - 2 .$

At leading order, we can further split F_1 into a "triangle" and a "box" contribution

$$F_1(\hat{s}, \hat{t}, m_h^2, m_t^2, D) = F_\triangle(\hat{s}, \hat{t}, m_h^2, m_t^2, D) + F_\square(\hat{s}, \hat{t}, m_h^2, m_t^2, D) . \tag{2.5}$$

As the LO form factor $F_\triangle$ only contains the triangle diagrams, which have no angular momentum dependence, it can be attributed entirely to an s-wave contribution. The form factors $F_\square$ and F_2 can be attributed to the spin-0 and spin-2 states of the scattering amplitude, respectively.

We can get an idea about the angular dependence of F_1 and F_2 by considering the partial wave decomposition of the scattering amplitude, which is independent of the loop order. It should be noted however that this analysis is valid for $2 \to 2$ scattering. At NLO, the cross section for the process $gg \to HH$ also contains a $2 \to 3$ scattering contribution from the real radiation. Therefore the analysis of the angular dependence below does not apply to the full NLO cross section.

In general, for a scattering process $a + b \to c + d$ with the corresponding helicities $\lambda_a, \ldots, \lambda_d$, the partial wave decomposition reads [66–68]

$$\langle \theta \phi \lambda_c \lambda_d | T(E) | 0 0 \lambda_a \lambda_b \rangle = 16\pi \sum_J (2J + 1) \langle \lambda_c, \lambda_d | T^J(E) | \lambda_a, \lambda_b \rangle e^{i(s_i - s_f)\phi} d_{s_i, s_f}^J(\theta) , \tag{2.6}$$

with $s_i = \lambda_a - \lambda_b$ and $s_f = \lambda_c - \lambda_d$, and where $\langle \theta \phi \lambda_c \lambda_d | T(E) | 0 0 \lambda_a \lambda_b \rangle$ denotes the transition matrix element. Unitarity must hold for each partial wave independently, i.e. $|T^J| \leq 1$. Thus the amplitude is decomposed into (orthogonal) Wigner d-functions $d^J_{s_i, s_f}(\theta)$, where J denotes the total angular momentum and s_i, s_f the total spin of the initial and final state, respectively. The structure of the amplitude is such that F_1 only contributes to $s_i = 0$, while F_2 only contributes to $s_i = 2$. F_1 has a component proportional to $d^0_{0,0}(\theta)$ as well as components proportional to $d^J_{0,0}(\theta)$ with $J \geq 2$, while the leading contribution to F_2 starts at $d^2_{2,0}(\theta)$. The partial waves for $J > 2$ are suppressed. The d-functions $d^J_{0,0}(\theta)$ are proportional to the Legendre-Polynomials $P_J(\cos \theta)$. As $P_0(x) = 1, P_2(x) = \frac{1}{2}(3x^2 - 1)$ and $d^2_{2,0}(\theta) \sim \sin^2 \theta$, we can conclude that the leading angular dependence of F_2 should be $\sim \sin^2 \theta$. From the analytic expression for F_2 at leading order [52], we can verify that indeed $F_2 \sim p_T^2 = (\hat{u}\,\hat{t} - m_h^4)/\hat{s} = \frac{\hat{s}}{4}\beta_h^2 \sin^2 \theta$ where $\beta_h^2 = 1 - 4m_h^2/\hat{s}$.

Further, using again the fact that the leading contributions to the amplitude come from the lower partial waves in eq. (2.6), we also conclude that the contribution from F_2 should be subleading with respect to F_1 in most of the kinematic regions. Indeed we observe that the contribution of the form factor F_2 to the virtual two-loop amplitude is suppressed as compared to F_1.

2.2 Leading order cross section

The functions F_i at leading order with full mass dependence can be found e.g. in refs. [52, 53]. At LO, the "triangle" form factor has the simple form

$$F_\triangle = C_\triangle \bar{F}_\triangle \,,\; C_\triangle = \frac{\lambda_{hhh}}{\hat{s} - m_h^2}\,,\; \lambda_{hhh} = 3m_h^2 \lambda\,, \tag{2.7}$$

$$\bar{F}_\triangle = 4m_q^2 \left\{ 2 + (4\,m_q^2 - \hat{s})C_0 \right\} = 2\hat{s}\,\tau_q \left[1 + (1 - \tau_q)f(\tau_q) \right]\,,$$

where $\lambda = 1$ in the Standard Model, $\tau_q = 4\,m_q^2/\hat{s}$ and

$$f(\tau_q) = \begin{cases} \arcsin^2 \dfrac{1}{\sqrt{\tau_q}} & \text{for } \tau_q \geq 1 \\ -\dfrac{1}{4}\left[\log \dfrac{1 + \sqrt{1 - \tau_q}}{1 - \sqrt{1 - \tau_q}} - i\pi \right]^2 & \text{for } \tau_q < 1 \end{cases} \tag{2.8}$$

$$C_0 = \int \frac{d^4 q}{i\pi^2} \frac{1}{(q^2 - m_q^2)\left[(q + p_1)^2 - m_q^2\right]\left[(q + p_1 + p_2)^2 - m_q^2\right]}\,. \tag{2.9}$$

The partonic leading order cross section for $gg \to hh$ can be written as

$$\hat{\sigma}^{\text{LO}}(gg \to hh) = \frac{\alpha_s^2(\mu_R)}{2^{12}v^4(2\pi)^3\hat{s}^2} \int_{\hat{t}_-}^{\hat{t}_+} d\hat{t} \left\{ |F_1|^2 + |F_2|^2 \right\}\,. \tag{2.10}$$

The integration limits $\hat{t}^\pm$ are derived from a momentum parametrisation in the centre-of-mass frame, leading to $\hat{t}_\pm = m_h^2 - \frac{\hat{s}}{2}(1 \mp \beta_h)$, where $\beta_h^2 = 1 - 4\frac{m_h^2}{\hat{s}}$.

To obtain the hadronic cross section, we also have to integrate over the PDFs. Defining the luminosity function as

$$\frac{d\mathcal{L}_{ij}}{d\tau} = \sum_{ij} \int_\tau^1 \frac{dx}{x} f_i(x, \mu_F) f_j\left(\frac{\tau}{x}, \mu_F\right)\,, \tag{2.11}$$

– 5 –

the total cross section reads

$$\sigma^{\mathrm{LO}} = \int_{\tau_0}^{1} d\tau \; \frac{d\mathcal{L}_{gg}}{d\tau} \; \hat{\sigma}^{\mathrm{LO}}(\hat{s} = \tau s) \,, \tag{2.12}$$

where s is the square of the hadronic centre of mass energy, $\tau_0 = 4m_h^2/s$, and μ_F is the factorization scale.

2.2.1 Heavy top limit

In the $m_t \to \infty$ approximation the LO form factors are given by

$$\bar{F}_\triangle \to \frac{4}{3}\hat{s} \,, \; F_\square \to -\frac{4}{3}\hat{s} \,, \; F_2 \to 0 \,, \tag{2.13}$$

which implies for the the effective ggH and $ggHH$ couplings c_h and c_{hh},[1]

$$c_h = -c_{hh} = -\frac{\alpha_s}{4\pi}\frac{i}{3} + \mathcal{O}\left(\frac{m_h^2}{4m_t^2}\right) \,. \tag{2.14}$$

From the expressions above we can derive the following expression for the squared amplitude in the heavy top limit:

$$|\mathcal{M}|^2 \sim \frac{2}{9} - \frac{4}{3}\,m_h^2\,\frac{\lambda}{\hat{s} - m_h^2} + 2\,m_h^4\,\frac{\lambda^2}{(\hat{s} - m_h^2)^2} \,. \tag{2.15}$$

For $\lambda = 1$, this expression vanishes at the Higgs boson pair production threshold $\hat{s} \sim 4m_h^2$. This explains why near the threshold the contributions containing the triple Higgs boson coupling and the ones which do not contain an s-channel Higgs boson exchange almost cancel. On the other hand, if the triple Higgs boson coupling was different from the Standard Model value, for example equal to zero, this should be clearly seen from the behaviour of the m_{hh} distribution. We investigate the effects of non-standard values for the triple Higgs boson coupling in section 3.3.

2.3 NLO cross section

The NLO cross section is composed of various parts, which we discuss separately in the following.

$$\sigma^{\mathrm{NLO}}(pp \to hh) = \sigma^{\mathrm{LO}} + \sigma^{\mathrm{virt}} + \sigma^{\mathrm{r}}_{gg} + \sigma^{\mathrm{r}}_{gq} + \sigma^{\mathrm{r}}_{g\bar{q}} + \sigma^{\mathrm{r}}_{q\bar{q}} \,. \tag{2.16}$$

The contributions from the real radiation, σ^{r}, can be divided into four channels, according to the partons in the initial state. The $q\bar{q}$ channel is infrared finite. Details are given in section 2.3.2.

---

[1]Higher order corrections to these effective couplings, and to couplings involving more than two Higgs bosons, can be found in ref. [69] and references therein.

2.3.1 Calculation of the virtual two-loop amplitude

Amplitude generation. For the virtual two-loop amplitude, we use projectors $P_j^{\mu\nu}$ to achieve a separation into objects carrying the Lorentz structure $T_i^{\mu\nu}$ and the form factors F_1 and F_2,

$$P_1^{\mu\nu}\mathcal{M}_{\mu\nu} = \frac{\alpha_s}{8\pi v^2} F_1(\hat{s}, \hat{t}, m_h^2, m_t^2, D) \,,$$
$$P_2^{\mu\nu}\mathcal{M}_{\mu\nu} = \frac{\alpha_s}{8\pi v^2} F_2(\hat{s}, \hat{t}, m_h^2, m_t^2, D) \,.$$

In D dimensions we can use the tensors $T_i^{\mu\nu}$, defined in eqs. (2.4), to build the projectors

$$P_1^{\mu\nu} = \frac{1}{4}\frac{D-2}{D-3} T_1^{\mu\nu} - \frac{1}{4}\frac{D-4}{D-3} T_2^{\mu\nu} \,, \tag{2.17}$$

$$P_2^{\mu\nu} = -\frac{1}{4}\frac{D-4}{D-3} T_1^{\mu\nu} + \frac{1}{4}\frac{D-2}{D-3} T_2^{\mu\nu} \,. \tag{2.18}$$

The virtual amplitude has been generated with an extension of the program GoSam [70, 71], where the diagrams are generated using Qgraf [72] and then further processed using Form [73, 74]. The two-loop extension of GoSam contains an automated python interface to Reduze [75], which implies that the user has to provide the integral families when running GoSam-2loop. The other input files needed by Reduze are generated automatically by GoSam-2loop, based on the kinematics of the given process. The reduction of the integrals occurring in the amplitude to master integrals should be performed separately, where in principle either of the codes Reduze [75], Fire5 [76] or LiteRed [77] can be used. Examples of two-loop diagrams contributing to Higgs boson pair production are shown in figure 2.

We would like to point out again that the distinction between "triangle diagrams" and "box diagrams" becomes ambiguous beyond the leading order. At two-loop and beyond there are diagrams which contain triangle sub-diagrams but which do not contain the Higgs boson self coupling, see figure 2(l).

Integral families and reduction. For the reduction of planar diagrams we have defined five integral families $\mathcal{F}_i$. Each family contains nine propagators which allows irreducible scalar products in the numerator to be written in terms of inverse propagators prior to reduction. In more detail, the occurring integrals have the form

$$I = \int \mathrm{d}^D k_1 \int \mathrm{d}^D k_2 \, N_{j_1}^{r_1} \dots N_{j_t}^{r_t} N_{j_{t+1}}^{-s_1} \dots N_{j_n}^{-s_{n-t}} \,, \tag{2.19}$$

where the N_j denote propagators of the generic form $1/(k^2 - m^2)$ with integer exponents $r_i \geq 1$ and $s_i \geq 0$. The maximal number of propagators forming denominators, i.e. with positive exponents r_i, in our case is $t_{\max} = 7$, and we find that integrals with up to four inverse propagators appear in the amplitude.

We chose a non-minimal set of integral families in favour of preserving symmetries as much as possible. The families are listed in table 1. The example diagrams shown in figure 2 can be assigned to the families as follows: diagrams (a), (j) and (l) to $\mathcal{F}_1$, diagrams (b) and (c) to $\mathcal{F}_2$, diagrams (e), (h) and (k) to $\mathcal{F}_3$, diagram (d) to $\mathcal{F}_4$, diagram (i) to $\mathcal{F}_5$.
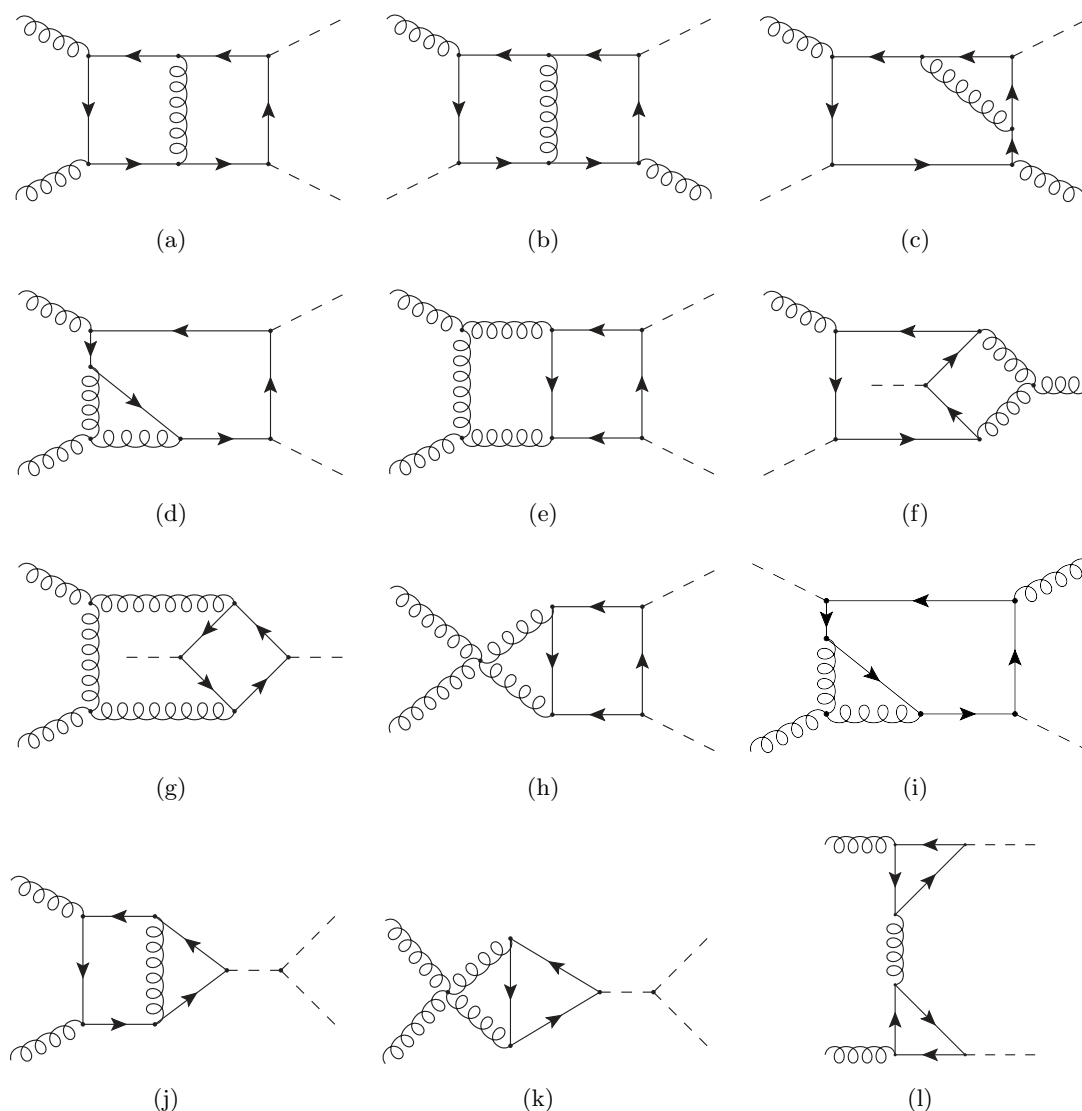
Figure 2. Examples of two-loop diagrams entering the virtual amplitude.

The amplitude generation leads to about 10000 integrals before any symmetries are taken into account. After accounting for symmetries and after reduction (complete reduction of the planar sectors and partial reduction of the non-planar ones), we end up with 145 planar master integrals plus 70 non-planar integrals, and a further 112 integrals that differ by a crossing. As these integrals contain four independent mass scales, $\hat{s}, \hat{t}, m_t^2, m_h^2$, only a small subset is known analytically. Besides the diagrams which are factorizing into two one-loop diagrams [59], the known integrals are the two-loop diagrams with two light-like legs and one massive leg, which enter single Higgs boson production, calculated e.g. in refs. [78–82], and the triangles with one light-like and two off-shell legs occurring in the two-loop calculation of $H \to Z\gamma$ [83, 84]. However, we calculate all integrals numerically using the program SECDEC [85–87].

$\mathcal{F}_1$	$\mathcal{F}_2$	$\mathcal{F}_3$
$k_1^2 - m_t^2$	$k_1^2 - m_t^2$	k_1^2
$k_2^2 - m_t^2$	$k_2^2 - m_t^2$	$(k_1 - k_2)^2 - m_t^2$
$(k_1 - k_2)^2$	$(k_1 - k_2)^2$	$(k_1 + p_1)^2$
$(k_1 + p_1)^2 - m_t^2$	$(k_1 + p_1)^2 - m_t^2$	$(k_2 + p_1)^2 - m_t^2$
$(k_2 + p_1)^2 - m_t^2$	$(k_2 + p_1)^2 - m_t^2$	$(k_1 - p_2)^2$
$(k_1 - p_2)^2 - m_t^2$	$(k_1 - p_3)^2 - m_t^2$	$(k_2 - p_2)^2 - m_t^2$
$(k_2 - p_2)^2 - m_t^2$	$(k_2 - p_3)^2 - m_t^2$	$(k_2 - p_2 - p_3)^2 - m_t^2$
$(k_1 - p_2 - p_3)^2 - m_t^2$	$(k_1 - p_2 - p_3)^2 - m_t^2$	$(k_1 + p_1 + p_3)^2$
$(k_2 - p_2 - p_3)^2 - m_t^2$	$(k_2 - p_2 - p_3)^2 - m_t^2$	$(k_2 + p_1 - p_2)^2$

$\mathcal{F}_4$	$\mathcal{F}_5$
$k_1^2 - m_t^2$	k_1^2
k_2^2	$k_2^2 - m_t^2$
$(k_1 - k_2)^2 - m_t^2$	$(k_1 - k_2)^2 - m_t^2$
$(k_1 + p_1)^2 - m_t^2$	$(k_1 + p_1)^2$
$(k_2 + p_1)^2$	$(k_2 + p_1)^2 - m_t^2$
$(k_1 - p_2)^2 - m_t^2$	$(k_1 - p_3)^2$
$(k_2 - p_2)^2$	$(k_2 - p_3)^2 - m_t^2$
$(k_1 - p_2 - p_3)^2 - m_t^2$	$(k_1 - p_2 - p_3)^2$
$(k_2 - p_2 - p_3)^2$	$(k_2 - p_2 - p_3)^2 - m_t^2$

Table 1. Integral families for the reduction of the planar diagrams. The non-planar integrals were computed as tensor integrals.

As the integral basis is not unique, we choose to have two set-ups, relying on different sets of basis integrals. This serves as a strong check of the calculation of the virtual amplitude. It has previously been noted that using a finite basis [88] along with sector decomposition can increase the precision obtained by numerical integration for a given number of sampling points [89]. We also observed that switching to a finite basis in some of the planar sectors turned out to be beneficial for the numerical evaluation of the master integrals.

A complete reduction could not be obtained for the non-planar 4-point integrals. The inverse propagators appearing in unreduced integrals were rewritten in terms of scalar products such that the resulting integrals had the lowest possible tensor rank. The tensor integrals (up to rank 4) were then directly computed with SecDec.

We would like to mention that non-planar diagrams also contribute to the leading colour coefficient. Therefore we could not identify a contribution which is both dominant and gauge invariant where only planar integrals contribute.

Renormalization. We expand the amplitude in $a_0 = \alpha_0/(4\pi)$, where α_0 is the bare QCD coupling. The bare amplitude can be written as

$$\mathcal{A}_B = a_0 \mathcal{A}_B^{(1)} + a_0^2 \mathcal{A}_B^{(2)} + \mathcal{O}(a_0^3), \tag{2.20}$$

where the one- and two-loop coefficients are given by

$$\mathcal{A}_B^{(1)} = S_\epsilon \mu_0^{2\epsilon} \left[\tilde{b}_0^{(1)} + \tilde{b}_1^{(1)}\epsilon + \tilde{b}_2^{(1)}\epsilon^2 + \mathcal{O}(\epsilon^3) \right], \tag{2.21}$$

$$\mathcal{A}_B^{(2)} = S_\epsilon^2 \mu_0^{4\epsilon} \left[\frac{\tilde{b}_{-2}^{(2)}}{\epsilon^2} + \frac{\tilde{b}_{-1}^{(2)}}{\epsilon} + \tilde{b}_0^{(2)} + \mathcal{O}(\epsilon) \right]. \tag{2.22}$$

Here μ_0^2 is a parameter introduced in dimensional regularisation to maintain a dimensionless bare coupling and $S_\epsilon = e^{-\gamma_E \epsilon}(4\pi)^\epsilon$, with γ_E the Euler constant. The one-loop amplitude is expanded to $\mathcal{O}(\epsilon^2)$ as it appears multiplied by the Catani-Seymour insertion operator stemming from the integrated dipoles, **I**, which has poles of $\mathcal{O}(\epsilon^{-2})$.

To renormalize the gluon wave function we must multiply the amplitude by $(Z_A)^{\frac{1}{2}}$ for each external gluon leg, where Z_A is the gluon field renormalization constant. We renormalize the QCD coupling using the relation

$$a_0 = a \, Z_a \left(\frac{\mu_R^2}{\mu_0^2} \right)^\epsilon , \; a = \frac{\alpha_s}{4\pi} \tag{2.23}$$

where α_s is the renormalized coupling and Z_a is the associated renormalization constant. Here μ_R is the renormalization scale and the dependence of α_s on μ_R is implicit. The top mass is renormalized by relating the bare top mass $m_{t_0}^2$ to the renormalized top mass m_t^2 via

$$m_{t_0}^2 = m_t^2 + a \, \delta m_t^2. \tag{2.24}$$

In practice, we compute top mass counter-term diagrams, treating $a \, \delta m_t^2$ as a counter-term insertion in top quark lines and renormalize the top Yukawa coupling using

$$y_{t_0} = \left(1 + a \frac{\delta m_t^2}{m_t^2} \right) y_t. \tag{2.25}$$

No Higgs wave function or mass renormalization is required as we compute only QCD corrections.

In our calculation we use conventional dimensional regularization (CDR) with $D = 4 - 2\epsilon$. We renormalize the top mass in the on-shell scheme and the QCD coupling in the $\overline{\text{MS}}$ five-flavour scheme ($N_f = 5$) with the top quark loops in the gluon self-energy subtracted at zero momentum.

The one-loop renormalization constants are given to first order in a by[2]

$$Z_A = 1 + a \, \delta Z_A + \mathcal{O}(a^2), \tag{2.26}$$

$$Z_a = S_\epsilon^{-1} \left[1 + a \, \delta Z_a + \mathcal{O}(a^2) \right], \tag{2.27}$$

where

$$\delta Z_A = \left(\frac{m_t^2}{\mu_R^2} \right)^{-\epsilon} \left(-\frac{4}{3\epsilon} T_R \right) ,$$

$$\delta Z_a = -\frac{1}{\epsilon} \beta_0 + \delta Z_a^{\text{hq}} , \; \beta_0 = \frac{11}{3} C_A - \frac{4}{3} T_R N_f^{\text{light}} ,$$

$$\delta Z_a^{\text{hq}} = \left(\frac{m_t^2}{\mu_R^2} \right)^{-\epsilon} \frac{4}{3\epsilon} T_R , \tag{2.28}$$

---

[2]Note that Z_a corresponds to the renormalization factor of the coupling g_s *squared*, therefore it is twice the expression for Z_{g_s} found in the literature, see e.g. eq. (3.4) of ref. [90].

and the mass counter-term in the on-shell scheme is given by

$$\delta m_t^2 = \left(\frac{m_t^2}{\mu_R^2}\right)^{-\epsilon} 2\, m_t^2\, C_F \left(-\frac{3}{\epsilon} - 4\right) + \mathcal{O}(\epsilon)\,. \tag{2.29}$$

The coefficients $\tilde{b}_i$ in (2.21), (2.22) contain integrals $I_{r,s}(\hat{s},\hat{t},m_h^2,m_t^2)$, where r denotes the number of propagators in the denominator and s denotes the number of propagators in the numerator and therefore defines the tensor rank of the integral, see also eq. (2.19). The integrals have mass dimension $[I_{r,s}] = D\,L - 2r + 2s$, with L the number of loops. We may therefore factor a dimensionful parameter M out of each integral such that they depend only on dimensionless ratios

$$I_{r,s}(\hat{s},\hat{t},m_h^2,m_t^2) = (M^2)^{-L\epsilon}(M^2)^{2L-r+s} I_{r,s}\left(\frac{\hat{s}}{M^2}, \frac{\hat{t}}{M^2}, \frac{m_h^2}{M^2}, \frac{m_t^2}{M^2}\right)\,. \tag{2.30}$$

The renormalized amplitude may then be written as

$$\mathcal{A}^{\text{virt}} = \prod_{n_g} Z_A^{\frac{1}{2}}\, \mathcal{A}_B \left(a_0 \to a\, Z_a \left(\mu_R^2/\mu_0^2\right)^{\epsilon}, m_{t_0}^2 \to m_t^2 + a\,\delta m_t^2\right)$$

$$= a\mathcal{A}^{(1)} + a^2\left(\frac{n_g}{2}\delta Z_A + \delta Z_a\right)\mathcal{A}^{(1)} + a^2\delta m_t^2 \mathcal{A}^{ct,(1)} + a^2 \mathcal{A}^{(2)} + O(a^3), \tag{2.31}$$

$$\mathcal{A}^{(1)} = \left(\frac{\mu_R^2}{M^2}\right)^{\epsilon}\left[b_0^{(1)} + b_1^{(1)}\epsilon + b_2^{(1)}\epsilon^2 + \mathcal{O}(\epsilon^3)\right], \tag{2.32}$$

$$\mathcal{A}^{ct,(1)} = \left(\frac{\mu_R^2}{M^2}\right)^{\epsilon}\left[c_0^{(1)} + c_1^{(1)}\epsilon + \mathcal{O}(\epsilon^2)\right], \tag{2.33}$$

$$\mathcal{A}^{(2)} = \left(\frac{\mu_R^2}{M^2}\right)^{2\epsilon}\left[\frac{b_{-2}^{(2)}}{\epsilon^2} + \frac{b_{-1}^{(2)}}{\epsilon} + b_0^{(2)} + \mathcal{O}(\epsilon)\right], \tag{2.34}$$

where

$$\tilde{b}^{(L)} = (M^2)^{-L\epsilon}b^{(L)}\,, \quad \tilde{c}^{(L)} = (M^2)^{-L\epsilon}c^{(L)}. \tag{2.35}$$

Since δm_t^2 contains poles of $\mathcal{O}(\epsilon^{-1})$ the coefficient c of the top mass counter-term must be expanded to $\mathcal{O}(\epsilon)$. It is obtained by the insertion of a mass counter-term into the heavy quark propagators,

$$\Pi_{ab}^{\delta m}(p) = \frac{i\delta_{ac}}{\not{p} - m}\, (-i\delta m)\, \frac{i\delta_{cb}}{\not{p} - m}\,, \tag{2.36}$$

where a, b, c are colour indices in the fundamental representation. Alternatively, the mass counter-term can be obtained by taking the derivative of the one-loop amplitude with respect to m.

The coefficients b and c in (2.31) are calculated numerically. We have extracted the dependence of the coefficients on the renormalization scale and introduced a dependence on a new scale, M, which we keep fixed in our numerics.

For the infrared singularities stemming from the unresolved real radiation, we use the Catani-Seymour subtraction scheme [91]. The infrared poles of the virtual amplitude are

cancelled after combination with the **I**-operator, which is given by

$$\mathbf{I}_{gg}(\epsilon) = \frac{\alpha_s}{2\pi} \frac{(4\pi)^\epsilon}{\Gamma(1-\epsilon)} S_\epsilon^{-1} \left(\frac{\mu_R^2}{\hat{s}}\right)^\epsilon \cdot 2 \cdot \left\{ \frac{C_A}{\epsilon^2} + \frac{\beta_0}{2\epsilon} - C_A \frac{\pi^2}{3} + \frac{\beta_0}{2} + K_g \right\}, \quad (2.37)$$

where K_g is also defined by the Catani-Seymour subtraction scheme [91]. Inserting the **I**-operator into the Born amplitude leads to[3]

$$
\begin{aligned}
\mathcal{A}^{\text{IR ct}} &= \frac{1}{2} \cdot \mathbf{I}_{gg}(\epsilon) \otimes a\, \mathcal{A}^{(1)} \\
&= a^2 \left(\frac{\mu_R^2}{\hat{s}}\right)^\epsilon \left(\frac{\mu_R^2}{M^2}\right)^\epsilon \left(1 - \epsilon^2 \frac{\pi^2}{12}\right) \left\{ \frac{2\, C_A}{\epsilon^2} + \frac{\beta_0}{\epsilon} - C_A \frac{2\pi^2}{3} + \beta_0 + 2K_g \right\} \\
&\quad \times \left[b_0^{(1)} + b_1^{(1)}\epsilon + b_2^{(1)}\epsilon^2 \right],
\end{aligned}
\tag{2.38}
$$

where we again have extracted a factor $(M^2)^{-\epsilon}$ from the integrals contained in the one-loop amplitude. Using (2.31) and (2.38) we therefore have

$$
\begin{aligned}
\mathcal{A}^{\text{virt}} + \mathcal{A}^{\text{IR ct}} &= a\mathcal{A}^{(1)} + a^2 \left(\frac{\mu_R^2}{M^2}\right)^\epsilon \left\{ \delta m_t^2 \left[c_0^{(1)} + c_1^{(1)}\epsilon \right] + \left(\frac{\mu_R^2}{M^2}\right)^\epsilon \left[\frac{b_{-2}^{(2)}}{\epsilon^2} + \frac{b_{-1}^{(2)}}{\epsilon} + b_0^{(2)} \right] \right. \\
&\quad + \left[b_0^{(1)} + b_1^{(1)}\epsilon + b_2^{(1)}\epsilon^2 \right] \left[\left(\frac{\mu_R^2}{\hat{s}}\right)^\epsilon \left\{ \frac{2\, C_A}{\epsilon^2} + \frac{\beta_0}{\epsilon} + \text{fin.} \right\} - \frac{\beta_0}{\epsilon} \right] \Bigg\} \\
&= a\mathcal{A}^{(1)} + a^2 \left(\frac{\mu_R^2}{M^2}\right)^\epsilon \left\{ \frac{1}{\epsilon^2} \left[2\, C_A\, b_0^{(1)} + b_{-2}^{(2)} \right] \right. \\
&\quad + \frac{1}{\epsilon} \left[2\, C_A\, b_0^{(1)} \ln\left(\frac{\mu_R^2}{\hat{s}}\right) + b_{-2}^{(2)} \ln\left(\frac{\mu_R^2}{M^2}\right) + b_{-1}^{(2)} - 6m_t^2 C_F c_0^{(1)} + 2\, C_A\, b_1^{(1)} \right] \\
&\quad + b_0^{(1)}\, \beta_0 \ln\left(\frac{\mu_R^2}{\hat{s}}\right) + \ln\left(\frac{\mu_R^2}{M^2}\right) b_{-1}^{(2)} - \ln\left(\frac{\mu_R^2}{m_t^2}\right) 6m_t^2 C_F c_0^{(1)} \\
&\quad + 2\, C_A\, b_1^{(1)} \ln\left(\frac{\mu_R^2}{\hat{s}}\right) + C_A\, b_0^{(1)} \ln^2\left(\frac{\mu_R^2}{\hat{s}}\right) + \frac{b_{-2}^{(2)}}{2} \ln^2\left(\frac{\mu_R^2}{M^2}\right) \\
&\quad + \text{finite non-logarithmic terms} \Bigg\}.
\end{aligned}
\tag{2.39}
$$

By construction the double pole in ϵ must vanish, thus (2.39) implies

$$b_{-2}^{(2)} = -2\, C_A\, b_0^{(1)}. \tag{2.40}$$

Substituting the above relation back into (2.39) we see that the dependence on the renormalization scale μ_R cancels in the single pole term. The dependence of the cross section on the factorization scale is encoded in the **P** and **K** terms of the Catani-Seymour framework [91].

---

[3]The factor of $\frac{1}{2}$ is necessary to cancel the factor of 2 obtained from squaring $\mathcal{A}^{\text{virt}} + \mathcal{A}^{\text{IR ct}}$ to get the cross section.

Integration of the two-loop amplitude. To evaluate the two-loop integrals appearing in the amplitude we first apply sector decomposition as implemented in SecDec. In the Euclidean region sector decomposition resolves singularities in the regulator ϵ, leaving only finite integrals over the Feynman parameters which can be evaluated numerically. In the physical region we treat the integrable singularities by contour deformation [86, 92–94]. To obtain the differential cross section we have to evaluate integrals at phase space points very close to threshold, where no special treatment is necessary but numerical convergence is considerably harder to achieve.

After sector decomposition each loop-integral I_j can be written as a sum over sectors s which have a Laurent series starting at some ϵ-order $e_s^{\min}$

$$I_j(\epsilon) = \sum_s \sum_{e > e_s^{\min}} \epsilon^e I_{j,s,e}. \tag{2.41}$$

For the numerical evaluation of the amplitude we structured the code such that the integrand of each sector-decomposed loop integral $I_{j,s,e}$ is stored along with the Laurent series of their coefficients a_j appearing in the expressions for the amplitudes (2.32)–(2.34). E.g. at two-loop we write the amplitude as

$$\mathcal{A}^{(2)} = \left(\frac{\mu_R^2}{M^2}\right)^{2\epsilon} \sum_{j,s,e} I_{j,s,e} \cdot a_j(\epsilon) \tag{2.42}$$

and store a_j as a vector containing the coefficients of I_j in the expressions for $b_k^{(2)}$, leading to the amplitude structure given in eq. (2.34).

Structuring the code this way allows us to dynamically set the number of sampling points used for each integral according to its contribution to the amplitude. After calculating each integral with a fixed number of sampling points, we assume that the integration error Δ_j of the integrals scales as $\Delta_j \propto t_j^{-\alpha}$ with the integration time t_j. To efficiently calculate the results $b_k^{(i)}$ with a given relative accuracy $\varepsilon_k^{(i)} = \Delta_k^{(i)}/b_k^{(i)}$, we estimate the required number of sampling points for each integral such that the total time

$$T_k^{(i)} = \sum_j t_j + \bar{\lambda} \left((\Delta_k^{(i)})^2 - \sum_j (\Delta_{j,k}^{(i)})^2 \right) \tag{2.43}$$

is minimal. $\Delta_{j,k}^{(i)}$ is the error estimate of integral I_j including its coefficients in $b_k^{(i)}$ and $\bar{\lambda}$ is a Lagrange multiplier. Since the loop integrals can contribute to several results $b_k^{(i)}$, we apply the above optimization formula for each required order in ϵ and for both form factors. For each integral, we then use the maximum of the estimated number of required sampling points. Instead of directly evaluating each integral with the calculated number of sampling points, we limit the number of new sampling points and iterate this procedure to reach the desired accuracy, updating the estimated number of sampling points after each iteration. The desired accuracy for the finite part of the two-loop amplitude ($\varepsilon_0^{(2)}$) is set to 3% for form factor F_1 and (depending on the ratio F_2/F_1) to a value of 5-20% for form factor F_2.
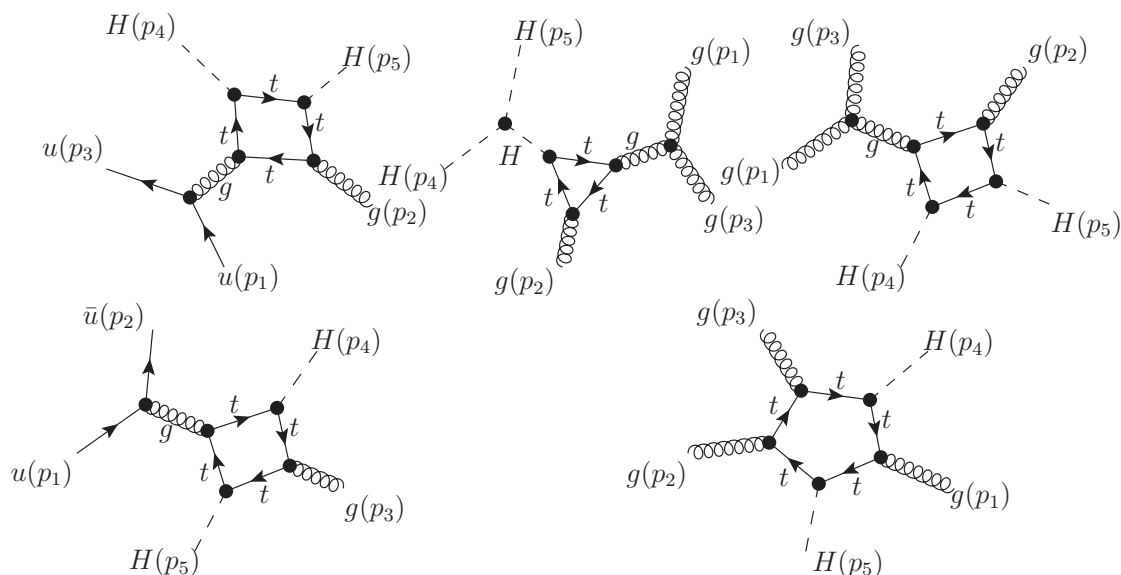
Figure 3. Examples of diagrams contributing to the real radiation part at NLO. The diagrams in the second row do not lead to infrared singularities.

For the integration we use a quasi-Monte Carlo method based on a rank-one lattice rule [95–97]. For suitable integrands, this rule provides a convergence rate of $\mathcal{O}(1/n)$ as opposed to Monte Carlo or adaptive Monte Carlo techniques, such as VEGAS [98], which converge $\mathcal{O}(1/\sqrt{n})$, where n is the number of sampling points. While we observe a convergence rate of $\mathcal{O}(1/n)$ for most of the integrals, the convergence of some integrals is worse and we therefore assume a scaling of $\Delta_j(t_j)$ with exponent $\alpha = 0.7$ when estimating the number of required sampling points.

The integration rule is implemented in OPENCL 1.1 and a further (OPENMP threaded) C++ implementation is used as a partial cross-check. The 913 phase-space points at 14 TeV (1029 phase-space points at 100 TeV) used for the current publication were computed with ∼16 dual NVIDIA TESLA K20X GPGPU nodes. More details on the numeric evaluation of the amplitudes can be found in refs. [99, 100].

2.3.2 Real radiation

As we calculate a process which is loop-induced, the NLO corrections involve two-loop integrals. But, for the real part only single-unresolved radiation can occur. This means that a standard NLO infrared subtraction scheme can be used. We use the Catani-Seymour dipole formalism [91], combined with a phase space restriction parameter α to restrict the dipole subtraction to a limited region, as suggested in ref. [101].

There are four partonic channels for the real radiation contribution to the cross section:

$$\sigma^{\mathrm{r}}(gg \to hh + g), \sigma^{\mathrm{r}}(gq \to hh + q), \sigma^{\mathrm{r}}(g\bar{q} \to hh + \bar{q}), \sigma^{\mathrm{r}}(q\bar{q} \to hh + g) . \qquad (2.44)$$

Including all crossings, there are 78 real radiation diagrams. Infrared singularities only originate from initial state radiation, diagrams with extra gluons radiated from a heavy quark line are infrared finite, which implies that the $q\bar{q}$ channel is finite. Example diagrams are depicted in figure 3.

2.4 Validation of the calculation and expansion in $1/m_t^2$

2.4.1 Expansion in $1/m_t^2$

We have calculated top mass corrections as an expansion in $1/m_t^2$ in the following way: we write the partonic differential cross section as

$$d\hat{\sigma}_{\text{exp},N} = \sum_{\rho=0}^{N} d\hat{\sigma}^{(\rho)} \left(\frac{\Lambda}{m_t}\right)^{2\rho}, \tag{2.45}$$

where $\Lambda \in \left\{\sqrt{\hat{s}}, \sqrt{\hat{t}}, \sqrt{\hat{u}}, m_h\right\}$, and determine the first few terms (up to $N = 3$) of this asymptotic series. The case $N = 0$ reproduces to the usual effective theory approach, without the need to calculate Wilson coefficients separately, however.

To generate the diagrams we again use QGRAF [72]. The generation and expansion of the amplitude in small external momenta is then performed using Q2E/EXP [102, 103] and leads to two-loop vacuum integrals inserted into tree-level diagrams as well as one-loop vacuum integrals inserted into massless one-loop triangles. Whereas the vacuum integrals are evaluated with MATAD [104], the massless integrals can be expressed in terms of a single one-loop bubble, which we achieve with the help of REDUZE [75]. Again, the algebraic processing of the amplitude is done with FORM [73, 74].

The exact and expanded matrix elements were combined in the following way: a series expansion for the virtual corrections was performed then rescaled with the exact born,

$$
\begin{aligned}
d\sigma^V + d\sigma^{LO}(\epsilon) \otimes \mathbf{I} &\approx d\sigma^V_{\text{exp},N} \frac{d\sigma^{LO}(\epsilon)}{d\sigma^{LO}_{\text{exp},N}(\epsilon)} + d\sigma^{LO}(\epsilon) \otimes \mathbf{I} \\
&= \left(d\sigma^V_{\text{exp},N} + d\sigma^{LO}_{\text{exp},N}(\epsilon) \otimes \mathbf{I}\right) \frac{d\sigma^{LO}(\epsilon)}{d\sigma^{LO}_{\text{exp},N}(\epsilon)} \\
&= \underbrace{\left(d\sigma^V_{\text{exp},N} + d\sigma^{LO}_{\text{exp},N}(\epsilon) \otimes \mathbf{I}\right)}_{\equiv V_N} \frac{d\sigma^{LO}(\epsilon = 0)}{d\sigma^{LO}_{\text{exp},N}(\epsilon = 0)} + \mathcal{O}(\epsilon).
\end{aligned} \tag{2.46}
$$

The first identity is valid because the colour structure of the exact and the expanded LO cross section are identical, and the second because the sum in the bracket is finite. Thus one needs to know only the ϵ dependence of the expanded LO cross section in this approximation.

There is some ambiguity when to do the rescaling, i.e. before or after the phase-space integration, and convolution with the PDFs. We opt to do it on a fully differential level, i.e. the rescaling is done for each phase-space point individually.

2.4.2 Checks of the calculation

We have verified for all calculated phase space points that the coefficients of the poles in ϵ are zero within the numerical uncertainties. For a randomly chosen sample of phase-space points we have calculated the pole coefficients with higher accuracy and obtained a median cancellation of five digits.

Our implementation of the virtual two-loop amplitude has been checked to be invariant under the interchange of $\hat{t}$ and $\hat{u}$ at various randomly selected phase-space points.

Single Higgs boson production has been re-calculated with the same setup for the virtual corrections and compared to the results obtained with the program SUSHI [105]. Further, the one-loop amplitude has been computed using an identical framework to the two-loop amplitude and has been checked against the result of ref. [52].

As a further cross-check we have also calculated top mass corrections as an expansion in $1/m_t^2$ as explained above. We have also compared to results provided to us by Jens Hoff for the orders $N = 4, 5, 6$ in the expansion above, worked out in [58]. The result of the comparison is shown in figure 4. One can see that below the $2m_t$ threshold, where agreement is to be expected, the expansion converges towards the full result.

The computation of the mass counter-term diagrams has been cross-checked by expanding the one-loop amplitude about the bare top mass

$$
\begin{aligned}
\mathcal{A}_B^{(1)}(m_t^2) &= \mathcal{A}_B^{(1)}(m_{t_0}^2) - a\delta m_t^2 \left(\frac{\partial}{\partial m_t^2} \mathcal{A}_B^{(1)}(m_t^2) \right)\Big|_{m_{t_0}^2} \\
&= \mathcal{A}_B^{(1)}(m_{t_0}^2) - a\delta m_t^2 \mathcal{A}_B^{ct,(1)}(m_{t_0}^2),
\end{aligned}
\tag{2.47}
$$

where $\mathcal{A}^{ct,(1)}$ is the one-loop top quark mass counter-term.

On the real radiation side, we have verified the independence of the amplitude from the phase space restriction parameter α. We have also varied the technical cut $p_T^{\min}$ in the range $10^{-2} \le p_T^{\min}/\sqrt{\hat{s}} \le 10^{-6}$ to verify that the contribution to the total cross section is stable and independent of the cut within the numerical accuracy.

Further, we have compared to the results of ref. [55] for the Born-improved HEFT and FT_{approx} approximations and found agreement within the numerical uncertainties [106].

3 Phenomenological results

3.1 Setup and total cross sections

We use the PDF4LHC15_nlo_100_pdfas [107–110] parton distribution functions, along with the corresponding value for α_s for both the NLO and the LO calculation. The masses have been set to $m_h = 125\,\text{GeV}$, $m_t = 173\,\text{GeV}$, and the top quark width has been set to zero. We use no cuts except a technical cut in the real radiation of $p_T^{\min} = 10^{-4}\sqrt{\hat{s}}$. The scale variation bands are the result of a 7-point scale variation [106] around the central scale $\mu_0 = m_{hh}/2$, with $\mu_{R,F} = c_{R,F}\,\mu_0$, where $c_R, c_F \in \{2, 1, 0.5\}$, except that the extreme variations $(c_R, c_F) = (2, 0.5)$ and $(c_R, c_F) = (0.5, 2)$ are omitted. The values we obtain for the total cross sections are shown in table 2. The full NLO result has a statistical uncertainty of 0.3% at 14 TeV (0.16% at 100 TeV) stemming from the phase space integration and an additional uncertainty stemming from the numerical integration of the virtual amplitude of 0.04% at 14 TeV and 0.2% at 100 TeV. These uncertainties are not included in table 2, where only scale variation uncertainties are shown.

3.2 NLO distributions

In this section we show differential distributions at $\sqrt{s} = 14\,\text{TeV}$ and $\sqrt{s} = 100\,\text{TeV}$ for various observables and compare to the approximate results in order to assess the effect of
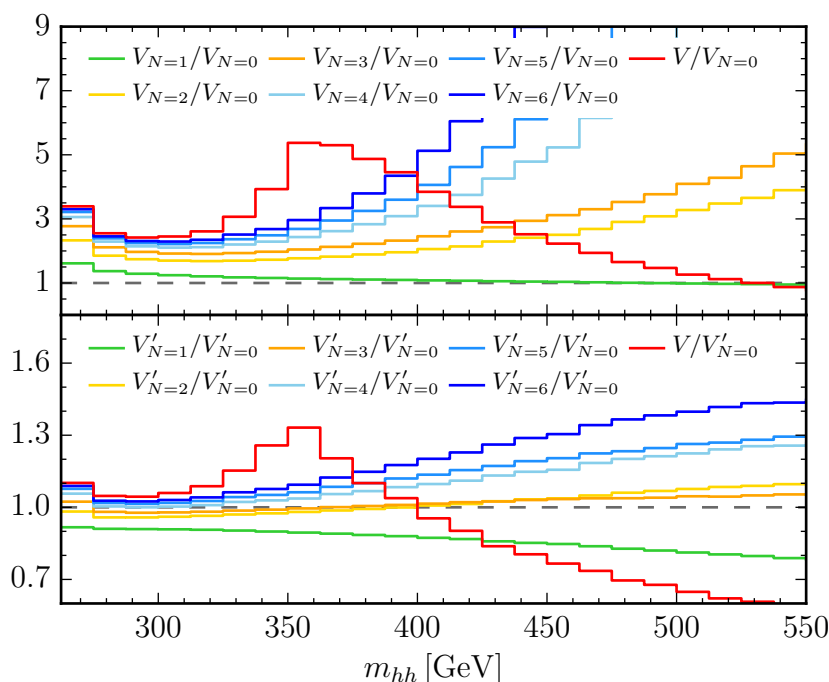
Figure 4. Comparison of the virtual part as defined in eq. (2.46) with full top-quark mass dependence to various orders in a $1/m_t^2$ expansion. V'_N denotes the Born-improved HEFT result to order N in the $1/m_t^2$ expansion, i.e. $V'_N = V_N B_{\mathrm{FT}}/B_N$. The results for the orders $N = 4, 5, 6$ have been provided to us by Jens Hoff [58].

$\sqrt{s}$	LO	B-i. NLO HEFT	NLO FT$_{\mathrm{approx}}$	NLO
14 TeV	$19.85^{+27.6\%}_{-20.5\%}$	$38.32^{+18.1\%}_{-14.9\%}$	$34.26^{+14.7\%}_{-13.2\%}$	$32.91^{+13.6\%}_{-12.6\%}$
100 TeV	$731.3^{+20.9\%}_{-15.9\%}$	$1511^{+16.0\%}_{-13.0\%}$	$1220^{+11.9\%}_{-10.7\%}$	$1149^{+10.8\%}_{-10.0\%}$

Table 2. Total cross sections at various centre of mass energies (in femtobarns). The uncertainty in percent is from 7-point scale variations as explained in the text. The central scale is $m_{hh}/2$. We used $m_t = 173\,\mathrm{GeV}$, $m_h = 125\,\mathrm{GeV}$. The PDF set is PDF4LHC15_nlo_100_pdfas.

the full top quark mass dependence at NLO. Results which are obtained within the effective field theory approach without reweighting by the leading order results in the full theory are always denoted by "basic HEFT", while "B-i. NLO HEFT" stands for the Born-improved NLO HEFT result, where the NLO corrections have been calculated in the $m_t \to \infty$ limit and then a reweighting factor $B_{\mathrm{FT}}/B_{\mathrm{HEFT}}$ is applied (on differential level, B_{FT} stands for the Born amplitude squared in the full theory).

We decided to take the same bin sizes as in ref. [64], such that the differences to the effective theory results can be exhibited most clearly. In figure 5 we show the Higgs boson pair invariant mass distribution m_{hh} at $\sqrt{s} = 14\,\mathrm{TeV}$ and $\sqrt{s} = 100\,\mathrm{TeV}$, comparing the full NLO result to various approximations. In particular, we compare to the "basic HEFT" approximation at $\sqrt{s} = 14\,\mathrm{TeV}$, showing that it fails to describe the distribution. Comparing the results at 14 TeV and 100 TeV, we observe that the differences of the full

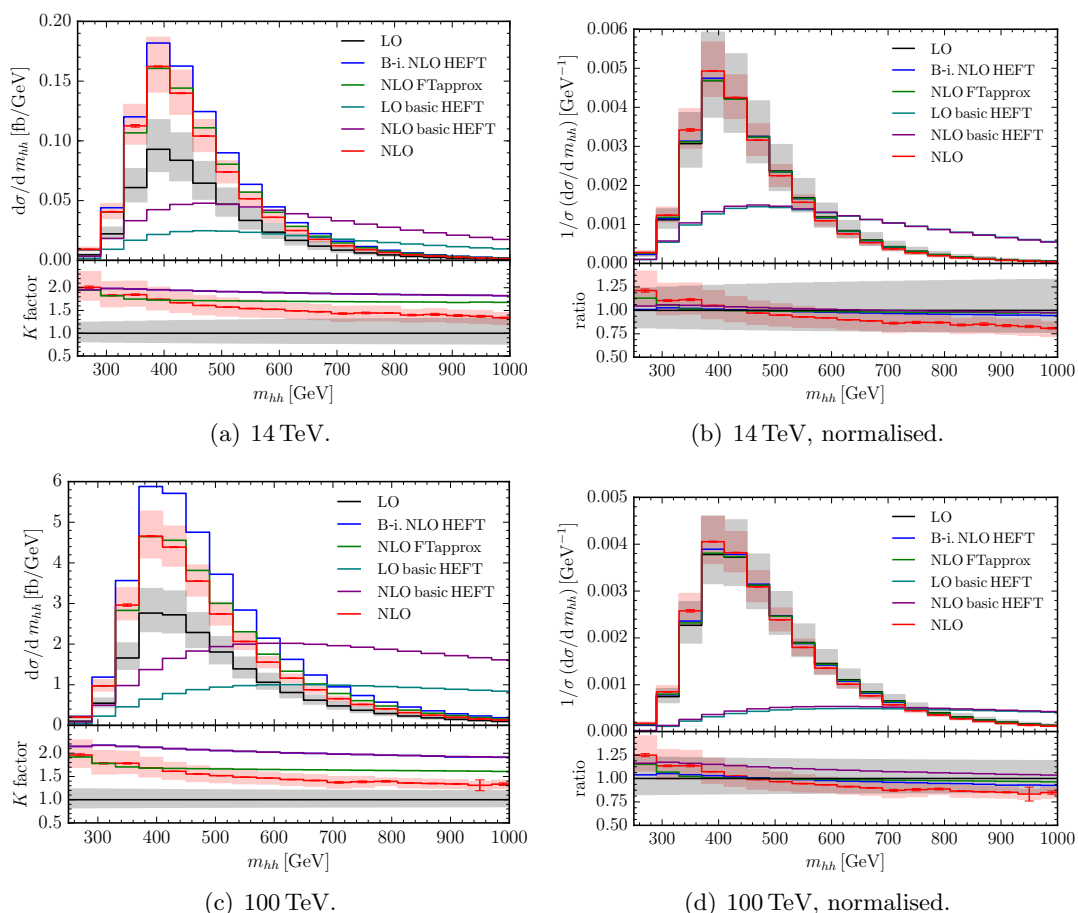**Figure 5**. Higgs boson pair invariant mass distribution m_{hh} at $\sqrt{s} = 14\,\text{TeV}$ and $\sqrt{s} = 100\,\text{TeV}$ for absolute values (left panels) and normalised to the corresponding total cross section (right panels).

NLO result to the Born-improved HEFT and also to the FT$_{\text{approx}}$ result are amplified at 100 TeV, as expected, as the HEFT approximation does not have the correct high energy behaviour. This scaling behaviour will be discussed more in detail below.

The K-factors are defined as the ratio of the NLO curve of the colour in the upper part of the plot to the corresponding LO result. This means that the "basic HEFT" curve is divided by the "basic HEFT" LO result. This is why the purple and the blue curves in figures 5 (a) and (c) lie on top of each other. We see that the K-factor is far from being uniform for the m_{hh} distribution, while the HEFT results suggest a uniform K-factor.

The ratio plots in figures 5 (b) and (d) are defined as the ratio of the curves normalized to their total cross section, shown in the upper plot, to the corresponding leading order result. As the purple curve in the upper plot is normalised to the total cross section in the basic HEFT approximation, while the blue curve is normalized to the Born-improved HEFT total cross section, the blue and the purple curves in the ratio plot do not coincide.

The $p_{T,h}$ distribution shown in figure 6 denotes the distribution of the "single inclusive" Higgs boson transverse momentum, which denotes the transverse momentum distribution of
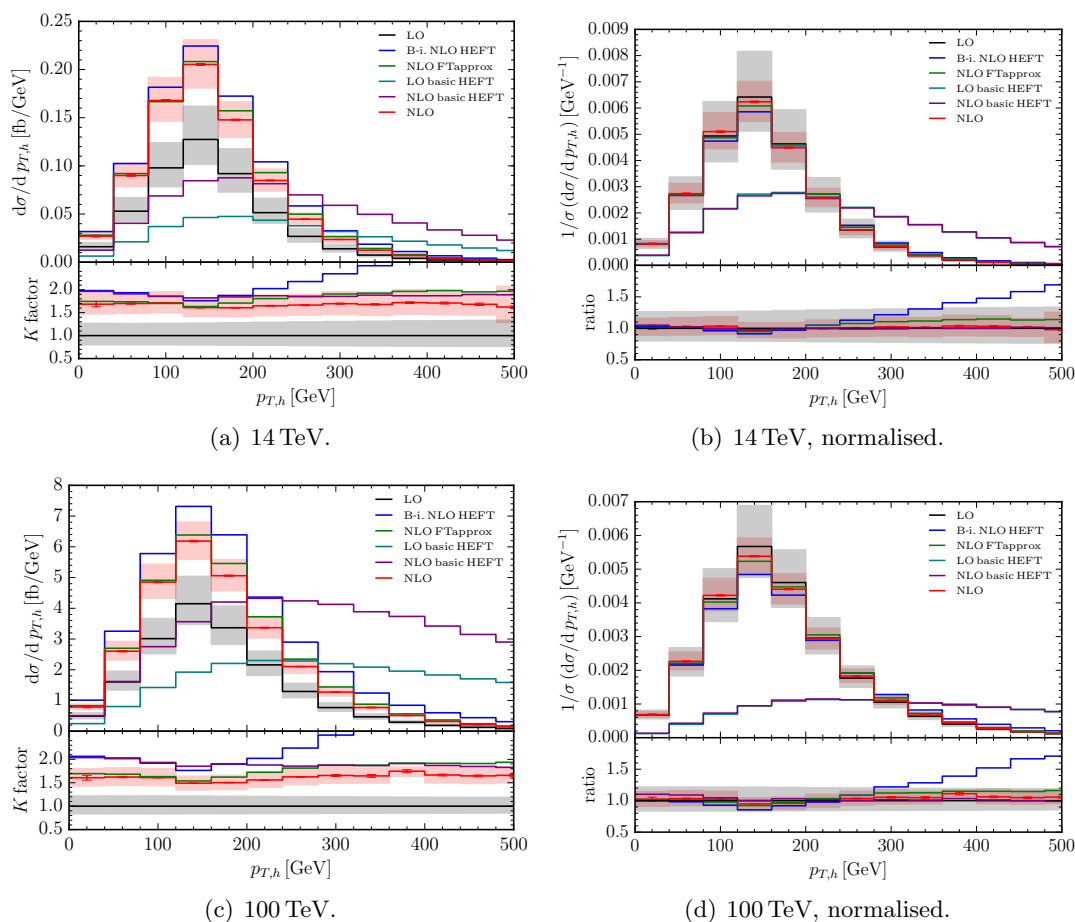
Figure 6. Transverse momentum distribution of (any) Higgs boson at $\sqrt{s} = 14\,\mathrm{TeV}$ and $\sqrt{s} = 100\,\mathrm{TeV}$.

any (randomly picked) Higgs boson. In contrast, figure 7 shows the transverse momentum distributions of the leading-p_T ("harder") and subleading-p_T ("softer") Higgs boson.

As in figure 5, the K-factors are defined as the ratio of the NLO curve of the colour in the upper part of the plot to the corresponding LO result, which means that the "basic HEFT" curve is divided by the "basic HEFT" LO result. However, in contrast to figure 5, the purple and the blue curves in figures 6 (a) and (c) do not lie on top of each other any longer. This is because there is some arbitrariness in the way the real radiation contribution, which has $2 \to 3$ kinematics, is rescaled at the differential level, i.e. for each individual phase space point, by the Born contribution, which has $2 \to 2$ kinematics. We use a mapping of the momenta which is a weighted average over the mappings used for the dipole subtraction terms for the re-weighting factor $d\sigma^{LO}_{\mathrm{FT}}/d\sigma^{LO}_{\mathrm{HEFT}}$ in the real radiation part. This mapping preserves the m_{hh} distribution, i.e. $d\sigma^{LO}$ calculated with the mapped momenta and calculated with the genuine $2 \to 2$ kinematics coincide in the m_{hh} case. For the transverse momentum distributions however, the dependence of the differential re-weighting factor on the momentum mappings is apparent, as the transverse momentum is closely related to the third final state particle.

It again becomes very clear that reweighting the basic HEFT result is indispensable in order to get at least somewhat close to the shape of the full NLO result. The $p_{T,h}$ distribution in figure 6(a) shows that, while the Born-improved NLO HEFT result starts moving out of the scale variation band of the full NLO result at 14 TeV beyond $p_{T,h} \sim m_t$, the FT$_{\mathrm{approx}}$ result stays within the scale uncertainty band of the full NLO result, (even though it is clear that it systematically overestimates the full result by about 20-30%). This is not surprising, as the tail of the $p_{T,h}$ distribution is to a large extent dominated by the real radiation contribution. At $\sqrt{s} = 100$ TeV, the FT$_{\mathrm{approx}}$ result leaves the scale variation band of the full NLO result beyond $p_{T,h} \sim 280$ GeV, but still is much closer to the full result than the Born-improved NLO HEFT result. The differences of the latter to the full result are amplified at 100 TeV.

In any case, it is clear that the scale variation bands can only be indicative of missing higher order corrections in perturbation theory, while the top quark mass effects (or the omission of the exact top quark mass dependence) are in a different category. Therefore one cannot expect that, for example, the NLO HEFT scale variation band would comprise the full NLO result. It is also worth mentioning that the "FT$'_{\mathrm{approx}}$" approximation [55], where the partial two-loop results (known from single Higgs production) were included, turned out to be a worse approximation than "FT$_{\mathrm{approx}}$", where the virtual part is given by the Born-improved NLO HEFT result, as it lead to a larger cross section than the "FT$_{\mathrm{approx}}$" one, and the latter is still larger than the full result.

Note that for $2 \to 2$ scattering the transverse momentum of the Higgs boson is given by $p_T^2 = \frac{\hat{s}}{4} \beta_h^2 \sin^2\theta$. Therefore, at leading order, the $p_{T,h}$ transverse momentum distribution directly reflects the angular dependence of the virtual amplitude. However, at NLO, the angular dependence of the form factors is influenced to a large extent by the real radiation. This can be seen from the distributions of the leading-p_T ("harder") and subleading-p_T ("softer") Higgs bosons shown in figure 7. The Higgs boson will pick up a large transverse momentum if it recoils against a hard jet, therefore the K-factor of the $p_{T,h}^{\mathrm{hard}}$ grows in the tail of the distribution, which is dominated by $2 \to 3$ kinematics.

Figure 8 shows the rapidity distributions of both the Higgs boson pair and the leading-p_T Higgs boson. As the mass effects are uniformly distributed over the whole rapidity range, the K-factors are close to uniform for these distributions, and the FT$_{\mathrm{approx}}$ result is within 10% of the full result. In figure 9 we display the tails of the m_{hh} and $p_{T,h}$ distributions on a logarithmic scale, in order to exhibit the scaling behaviour in the high energy limit. Using leading-log high energy resummation techniques, it can be shown [111] that at high transverse momentum, the differential partonic cross section for single Higgs (+jets) production $d\sigma/dp_{T,h} \sim 1/p_{T,h}^a$ scales with $a = 2$ in the full theory, however with $a = 1$ in the effective theory. This behaviour also has been recently confirmed by a (leading order) calculation of Higgs + 1,2,3 jet production with full mass dependence [112]. In order to investigate the high energy scaling behaviour we fitted a line to the tail of the leading order m_{hh} distribution (with the luminosity factor set to one, plotted logarithmically), and found the following scaling behaviour: with full mass dependence, the scaling is as m_{hh}^{-3} for $d\hat{\sigma}/dm_{hh}$ i.e. the partonic cross section scales as $\hat{s}^{-1}$, while in the basic HEFT approximation the scaling is as m_{hh} for $d\hat{\sigma}/dm_{hh}$ i.e. the partonic cross section grows as $\hat{s}$.
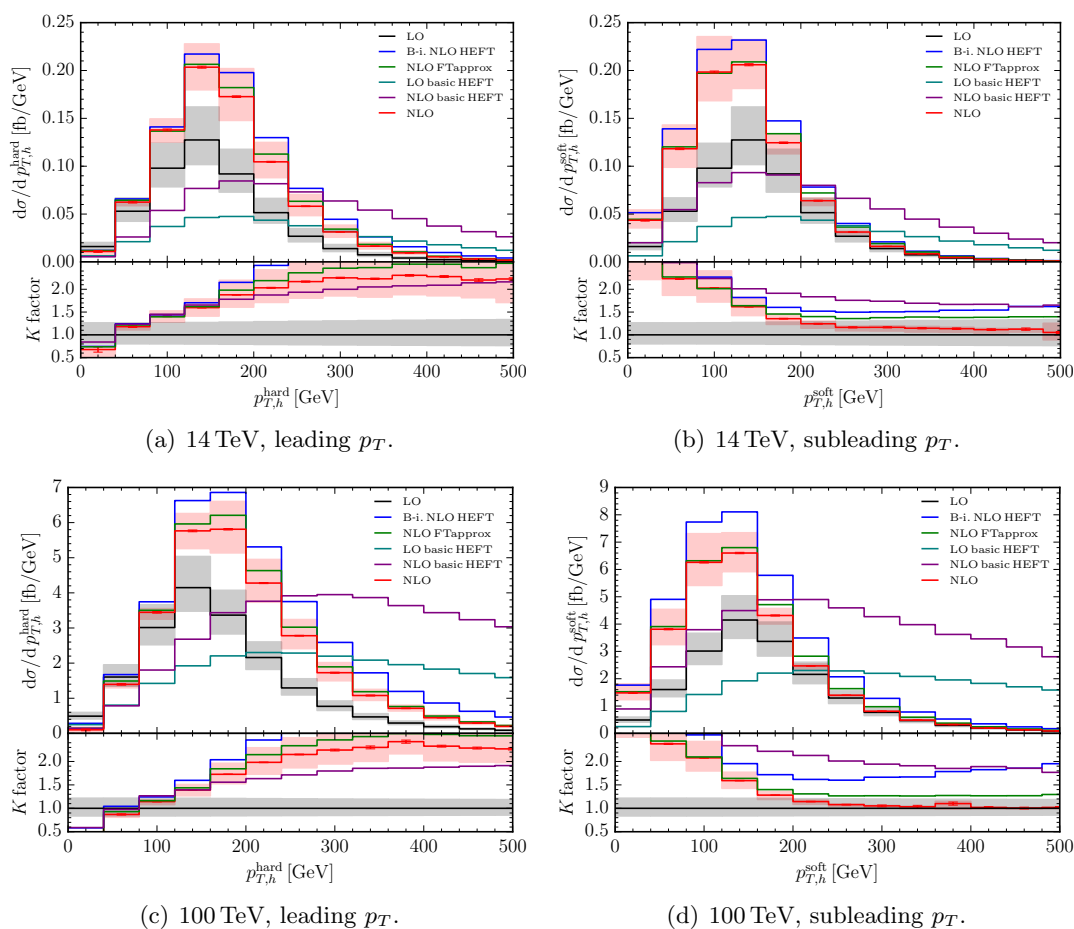
Figure 7. Transverse momentum distribution of the leading-p_T Higgs boson (left panels) and the subleading-p_T Higgs boson (right panels) at $\sqrt{s} = 14\,\mathrm{TeV}$ and $\sqrt{s} = 100\,\mathrm{TeV}$.

From figure 9 one can see that this relative difference in the high-energy scaling behaviour between the full calculation and the basic HEFT approximation is similar at NLO.

In figure 10 we show distributions for an improved FT$_{\mathrm{approx}}$, which is supplemented with higher order terms in the expansion of the virtual amplitude in $1/m_t^2$ as given by eq. (2.46), dubbed "exp. virt." for "expanded virtuals". We see a trend similar to the one for the virtual (plus **I**-operator) part shown in figure 4.

In order to better account for missing higher order corrections it is desirable to combine the full NLO with NNLO results obtained in the HEFT, ideally on a differential level. As a first attempt to achieve this, we take the NNLO to NLO ratio from ref. [64] and calculate

$$\mathrm{d}\sigma^{\,\mathrm{NLO\text{-}i.\,NNLO\ HEFT}} = \mathrm{d}\sigma^{\,\mathrm{NLO}} \frac{\mathrm{d}\sigma^{\,\mathrm{NNLO\ basic\ HEFT}}}{\mathrm{d}\sigma^{\,\mathrm{NLO\ basic\ HEFT}}} \tag{3.1}$$

bin by bin, where "NLO-i. NNLO HEFT" stands for NLO-improved NNLO HEFT. Results for various distributions are shown in figure 11. The error band is the NLO-rescaled scale uncertainty of the NNLO basic HEFT distributions, and the error on the central value is due to the error on the full NLO result. Applying the same naive rescaling on the total cross
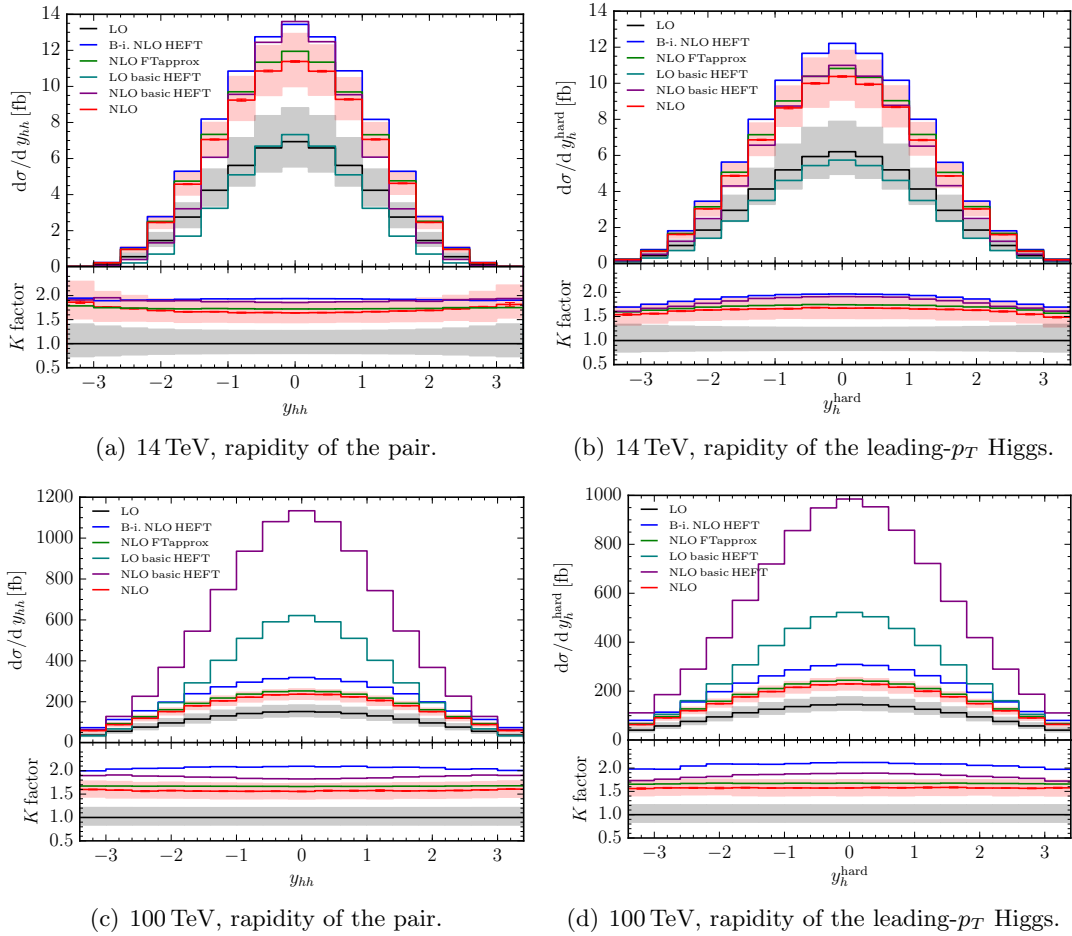
(a) 14 TeV, rapidity of the pair.

(b) 14 TeV, rapidity of the leading-p_T Higgs.

(c) 100 TeV, rapidity of the pair.

(d) 100 TeV, rapidity of the leading-p_T Higgs.

Figure 8. Rapidity distribution of the Higgs boson pair and the leading-p_T Higgs boson at $\sqrt{s} = 14$ TeV and $\sqrt{s} = 100$ TeV.
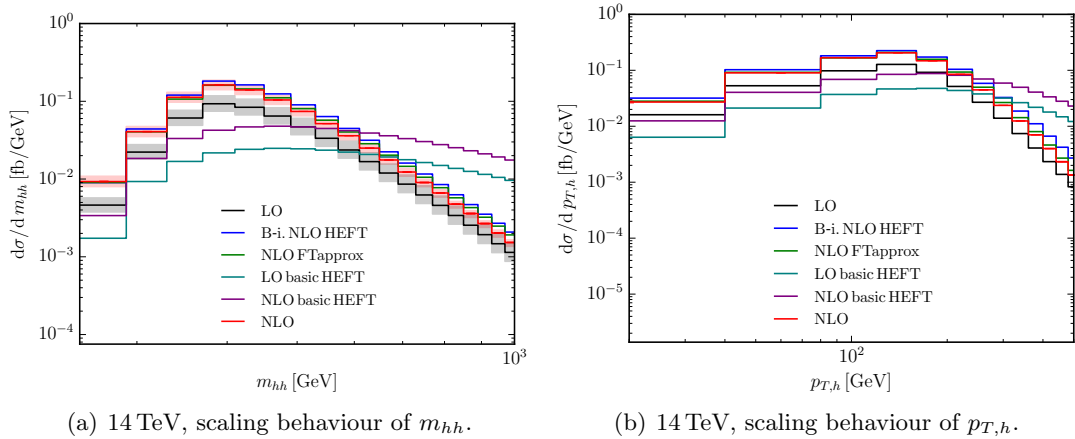

(a) 14 TeV, scaling behaviour of m_{hh}.

(b) 14 TeV, scaling behaviour of $p_{T,h}$.

Figure 9. Higgs boson pair invariant mass distribution (a) and transverse momentum distribution (b) at $\sqrt{s} = 14$ TeV on a logarithmic scale. The different high-energy scaling behaviour of the amplitude in the full and the basic HEFT calculation can be clearly seen in the tails of the distributions.

(a) 14 TeV, m_{hh}.

(b) 14 TeV, $p_{T,h}$.
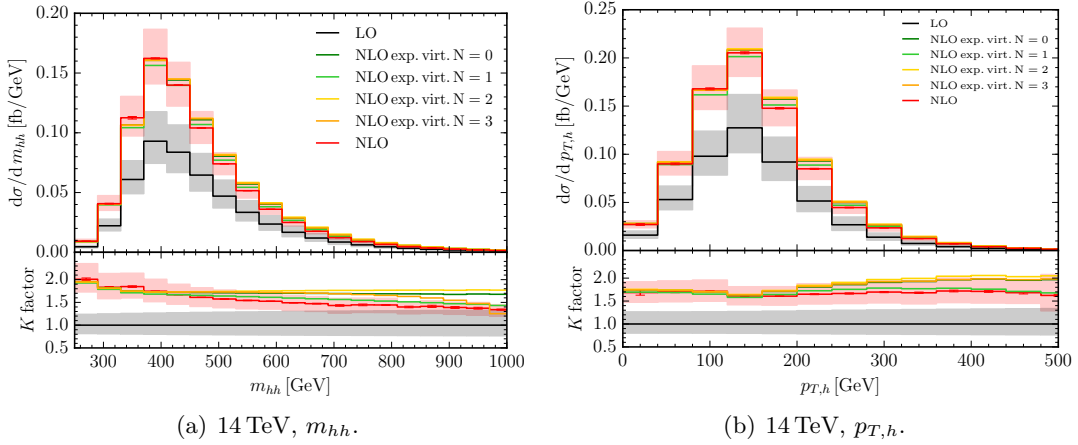
Figure 10. Invariant mass distribution of the Higgs boson pair (a) and p_T distribution of any Higgs (b) at $\sqrt{s} = 14\,\text{TeV}$ combining the full real emission with the virtual contribution expanded in $1/m_t^2$ up to order N. Note that $N = 0$ corresponds to $\text{FT}_{\text{approx}}$.
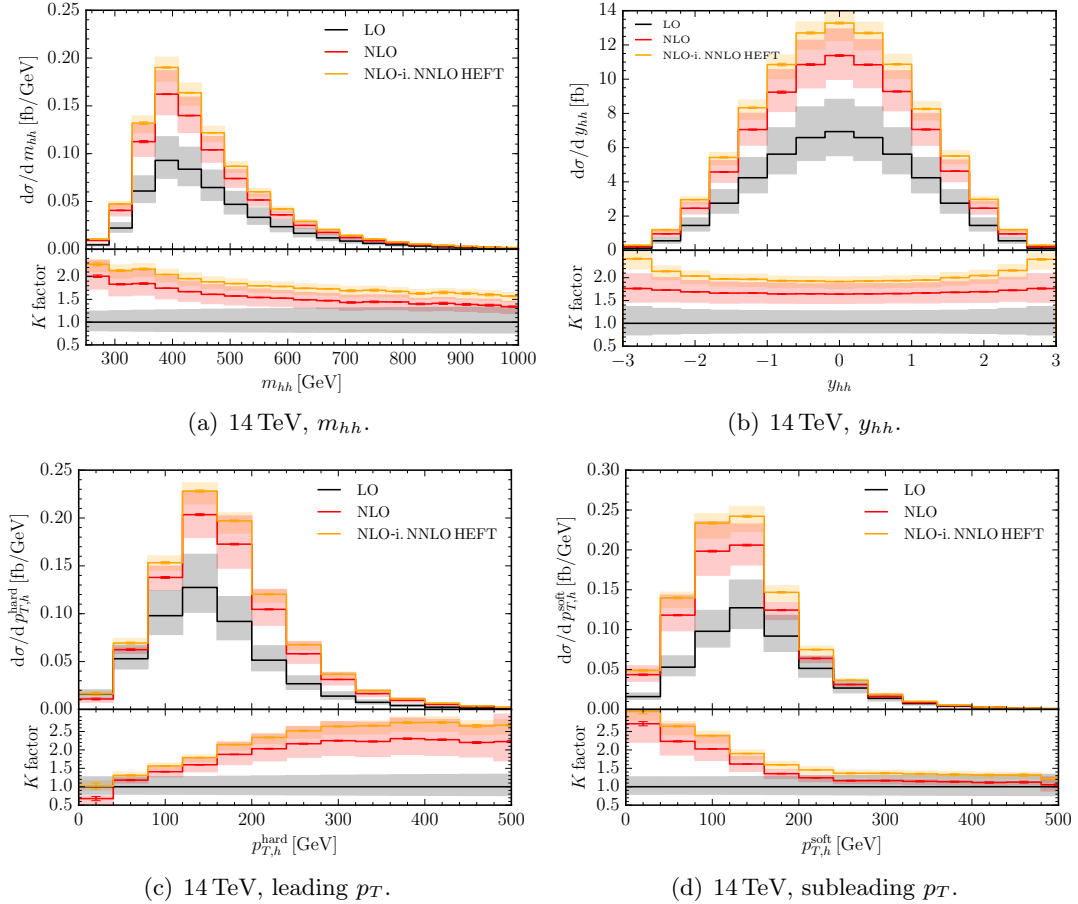

(a) 14 TeV, m_{hh}.

(b) 14 TeV, y_{hh}.

(c) 14 TeV, leading p_T.

(d) 14 TeV, subleading p_T.

Figure 11. Invariant mass (a) and rapidity distribution (b) of the Higgs boson pair and transverse momentum distribution of the leading-p_T (c) and the subleading-p_T Higgs boson (d) at $\sqrt{s} = 14\,\text{TeV}$ including the combination with the NNLO HEFT results from ref. [64] described in the main text.
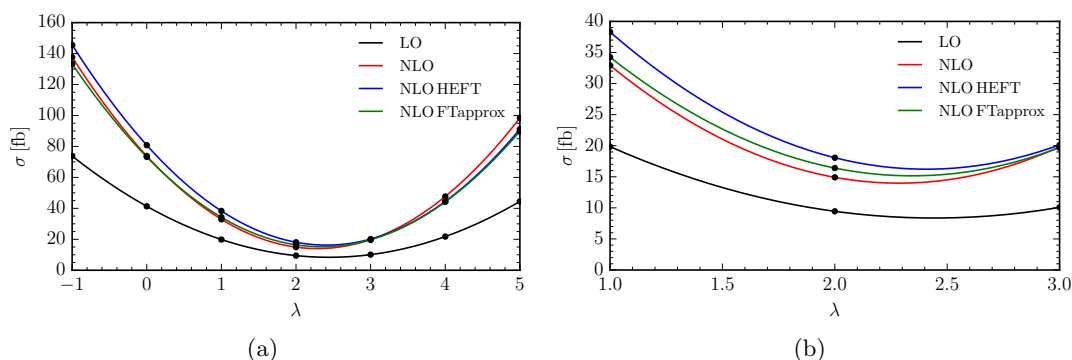
Figure 12. Total cross sections for various values of the triple Higgs coupling. Panel (b) zooms into the region around the minimum. The curves are the result of an interpolation of integer values for $\lambda \in \{-1, \ldots, 5\}$.

section, one obtains $\sigma^{\text{NLO-i. NNLO HEFT}} = 38.67^{+5.2\%}_{-7.6\%}$ for $14\,\text{TeV}$, where we have neglected the numerical errors and simply quote the relative scale uncertainty given in ref. [64] for the NNLO basic HEFT result.

3.3 Sensitivity to the triple Higgs coupling

As already mentioned in section 2.1, the Higgs boson self-coupling in the Standard Model is quite special. Not only that it is completely determined in terms of the Higgs boson mass and VEV, but it also leads to the fact that at the double Higgs production threshold $\sqrt{\hat{s}} = 2m_h^2$, the LO cross section is almost vanishing, due to destructive interference between box and triangle contributions. Therefore a measurement of the Higgs boson self-coupling is a very sensitive probe of New Physics effects.

A more complete analysis of such effects would require an approach where further operators are taken into account, for example operators which mediate direct $t\bar{t}HH$ couplings (and Higgs-gluon couplings which can differ from the SM HEFT ones), see e.g. [35, 38, 40]. However, the conclusions drawn from the calculation of NLO corrections in the $m_t \to \infty$ limit to the extended set of EFT Wilson coefficients have to be taken with a grain of salt, as the full top quark mass dependence may affect them considerably.

In this section we would like to focus on just a single line in the parameter space of possible non-SM Higgs couplings and investigate the behaviour of the m_{hh} distribution under variations of λ, where we have defined $\lambda_{hhh} = 3m_h^2\lambda$, see eq. (2.7).

In figure 12 we show the total cross section as a function of λ. As already observed for the LO cross section [23], it has a minimum around $\lambda = 2$. Negative λ values, which are not excluded neither theoretically nor experimentally (within certain broad limits given e.g. by vacuum stability), do not lead to destructive interference and therefore result in a much larger cross section. For large positive values, $\lambda \sim 5$, the total cross section is of comparable size to the one for $\lambda \simeq 0$, but the shape of the m_{hh} distribution is completely different. This can be seen in figure 13, where we show the Higgs boson pair invariant mass distribution for various values of the Higgs boson self-coupling, at $\sqrt{s} = 14\,\text{TeV}$ and $\sqrt{s} = 100\,\text{TeV}$. For $\lambda = 5$, the differential cross section is mainly dominated by contributions containing the Higgs boson self coupling and peaks at low m_{hh} values. In contrast, the $\lambda = 0$ case,
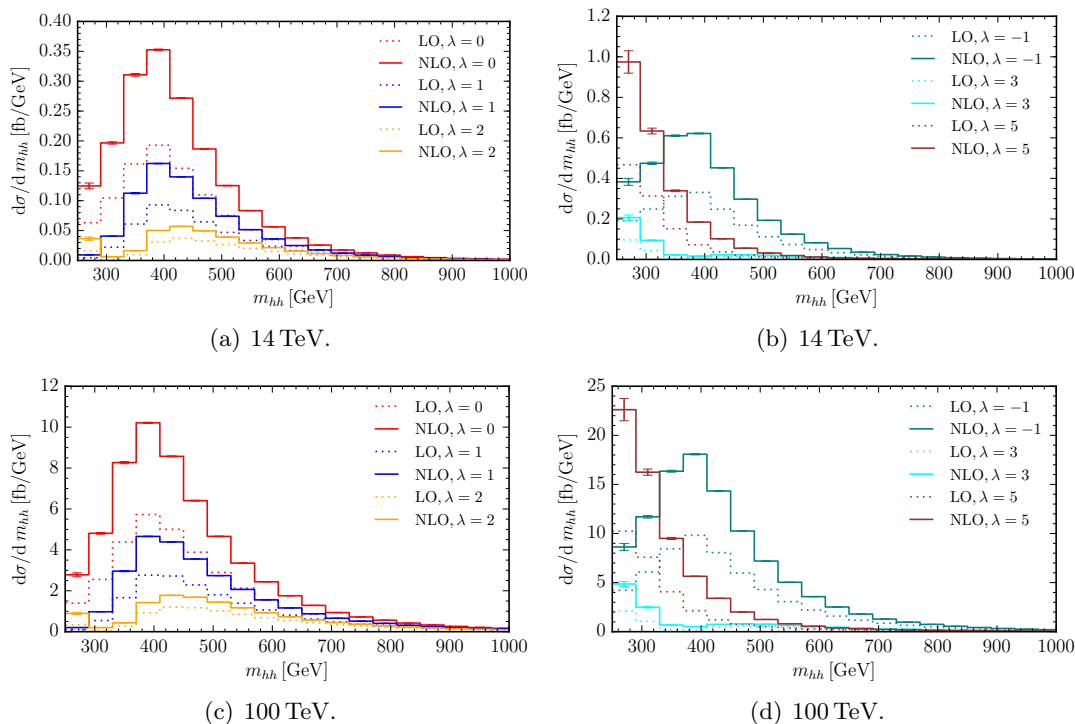
Figure 13. NLO and LO results with full top quark mass dependence for the m_{hh} distribution at 14 TeV and 100 TeV, for various values of the triple Higgs coupling, where $\lambda = 1$ corresponds to the Standard Model value.

which does not contain any triple Higgs coupling contribution, peaks shortly beyond the $2m_t$ threshold at $m_{hh} \sim 400\,\text{GeV}$, as does the case $\lambda = -1$. In the latter case, however, the total cross section is much larger. The case $\lambda = 2$ shows a dip at $m_{hh} \sim 300\,\text{GeV}$, which is due to destructive interference effects as mentioned above. At 100 TeV, the shape of the distributions is very similar. However, the fact that the cross sections are much larger can be exploited to place cuts which enlarge the sensitivity to the Higgs boson self coupling. For example, one can try to enhance the self-coupling contribution by cuts favouring highly boosted virtual Higgs bosons, decaying into a Higgs boson pair which could be detected in the $b\bar{b}\,b\bar{b}$ channel. A highly boosted virtual Higgs boson must recoil against a high-p_T jet. Therefore, an enhancement of the boosted component could be achieved by imposing a $p_{T,jet}^{\min}$ cut on the recoiling jet in Higgs boson pair plus jet production [113].[4] An additional advantage of boosted Higgs bosons is the fact that they lend themselves to the use of the $b\bar{b}b\bar{b}$ rather than the $b\bar{b}\gamma\gamma$ decay channel, as the decay channel into b-quarks is accessible through boosted techniques. This leads to a gain in the rate which easily makes up for the loss in statistics due to a high $p_{T,jet}^{\min}$ cut.

Figure 14 shows a comparison to the different approximations for various values of λ, as well as the K-factors. For all values of λ, the K-factors are far from being uniform, while the HEFT approximation suggests almost uniform K-factors for $\lambda \leq 1$. For $\lambda = 2$, we see a pronounced "interference dip" at $m_{hh} \sim 330\,\text{GeV}$, which is present at LO already.

---

[4]We thank Michelangelo Mangano for pointing this out.

We can get an idea about the destructive interference effect by observing the following: in the basic HEFT approximation, the squared Born amplitude is given by eq. (2.15). This expression has a double zero at $\hat{s} = m_h^2(1 + 3\lambda)$. Therefore, the re-weighting factor $B_{\mathrm{FT}}/B_{\mathrm{HEFT}}$ can get large when B_{HEFT} approaches zero, i.e. at $\sqrt{\hat{s}} \simeq 330.72\,\mathrm{GeV}$ for $\lambda = 2$, $\sqrt{\hat{s}} \simeq 395.29\,\mathrm{GeV}$ for $\lambda = 3$, $\sqrt{\hat{s}} \simeq 450.7\,\mathrm{GeV}$ for $\lambda = 4$ and $500\,\mathrm{GeV}$ for $\lambda = 5$. In the full theory, the amplitude does not vanish completely at these points, but nonetheless also gets small, which should be the reason for the dips in the m_{hh} distributions for $\lambda = 2$ and 3.

4   Conclusions

We have presented results of a fully differential calculation of Higgs boson pair production in gluon fusion at NLO retaining the exact top quark mass dependence. For the total cross section at $\sqrt{s} = 14\,\mathrm{TeV}$, we found a reduction of 14% compared to the Born improved HEFT, and a 24% reduction at $\sqrt{s} = 100\,\mathrm{TeV}$. For differential distributions, the mass effects can be even larger. In the tails of the Higgs boson transverse momentum distributions, the differences to the Born improved NLO HEFT approximation amount to more than 50%, while the $\mathrm{FT}_{\mathrm{approx}}$ result, where the full top mass dependence is included only in the real radiation part, stays within 20% of the full result. The basic NLO HEFT approximation, where no reweighting by the Born result in the full theory is performed, fails to properly describe the shape of the m_{hh} and p_{Th} distributions, in particular in the tails of the distributions. To quantify this well-known fact, we have performed an analysis of the high-energy scaling behaviour.

We also studied the influence of non-standard values for the Higgs boson self-coupling on the total cross sections and m_{hh} distributions. As is known from leading order, there is destructive interference between various contributions to the cross section, and this feature persists at NLO. Varying $\lambda_{hhh}/\lambda_{\mathrm{SM}}$ leads to a minimum in the value for the total cross section around $\lambda_{hhh}/\lambda_{\mathrm{SM}} \sim 2.3$. The shape of the m_{hh} distribution is rather sensitive to variations of λ_{hhh}, which alter the interference pattern. For example, at $\lambda_{hhh} = 0$, the total cross section is almost as large as for $\lambda_{hhh}/\lambda_{\mathrm{SM}} = 5$, but the shape of the distributions is very different.

Further, we made a first attempt to combine the full NLO results with the NNLO results calculated in the basic HEFT approximation [64] at differential distribution level, which should lead to a "NLO-improved NNLO HEFT" result, which may still be improved in the near future in various directions, for example towards Higgs boson decays.
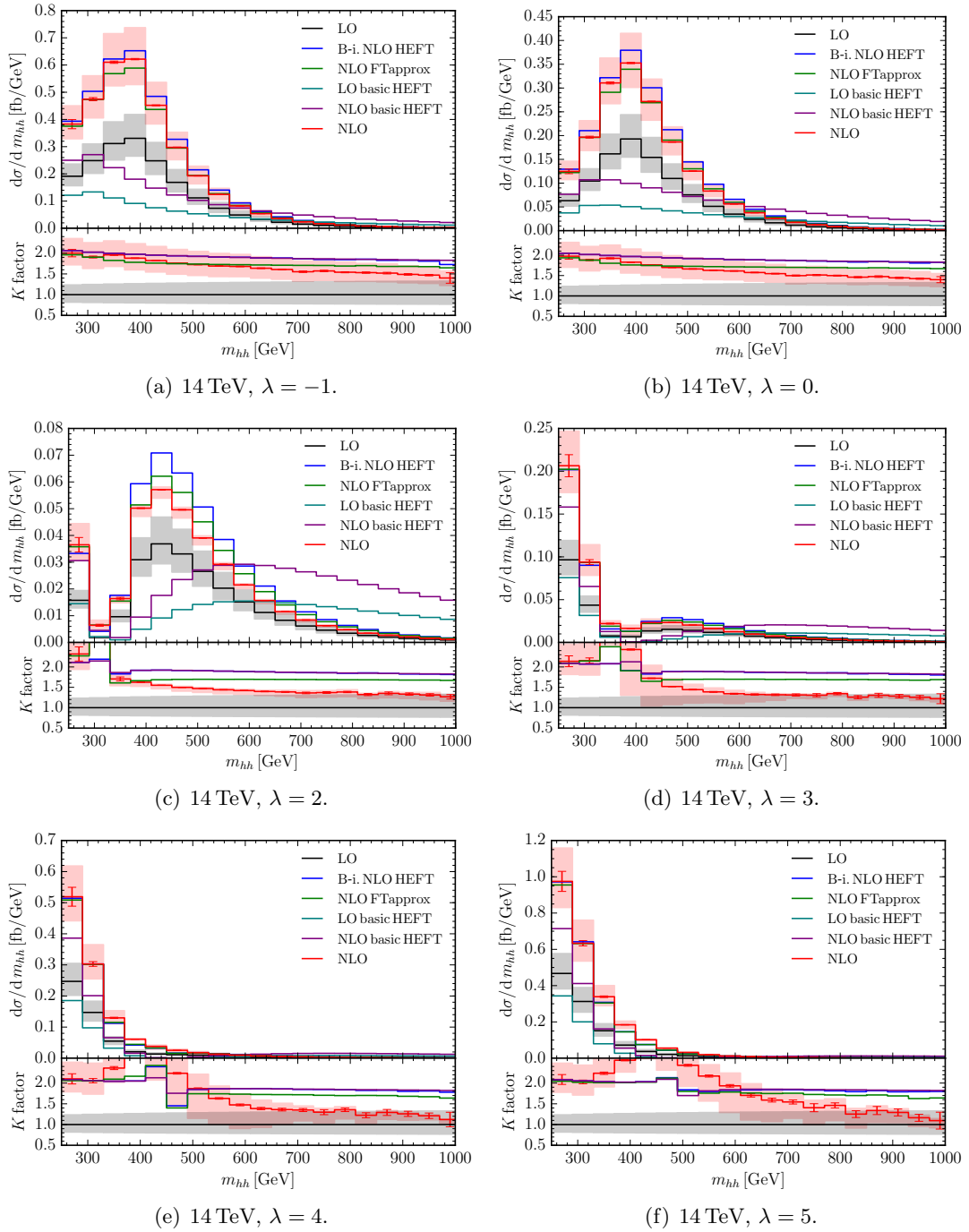
Acknowledgments

Figure 14. Higgs boson pair invariant mass distribution m_{hh} at $\sqrt{s} = 14\,\text{TeV}$ for non-standard values of the triple Higgs coupling.

References

[1] ATLAS collaboration, *Observation of a new particle in the search for the standard model Higgs boson with the ATLAS detector at the LHC*, [*Phys. Lett.* **B 716** (2012) 1](#) [[arXiv:1207.7214](#)] [[INSPIRE](#)].

[2] CMS collaboration, *Observation of a new boson at a mass of* 125 *GeV with the CMS experiment at the LHC*, [*Phys. Lett.* **B 716** (2012) 30](#) [[arXiv:1207.7235](#)] [[INSPIRE](#)].

[3] ATLAS, CMS collaboration, G. Aad et al., *Combined measurement of the Higgs boson mass in pp collisions at* $\sqrt{s} = 7$ *and* 8 *TeV with the ATLAS and CMS experiments*, [*Phys. Rev. Lett.* **114** (2015) 191803](#) [[arXiv:1503.07589](#)] [[INSPIRE](#)].

[4] ATLAS collaboration, *Higgs pair production in the* $H(\to \tau\tau)H(\to b\bar{b})$ *channel at the high-Luminosity LHC*, [ATL-PHYS-PUB-2015-046](#) (2015).

[5] ATLAS collaboration, *Prospects for measuring Higgs pair production in the channel* $H(\to \gamma\gamma)H(\to b\bar{b})$ *using the ATLAS detector at the HL-LHC*, [ATL-PHYS-PUB-2014-019](#) (2014).

[6] C. Dontardo et al., *Technical proposal for the Phase-II upgrade of the CMS detector*, [CERN-LHCC-2015-010](#) (2015).

[7] ATLAS collaboration, *Search for Higgs boson pair production in the* $b\bar{b}\gamma\gamma$ *final state using pp collision data at* $\sqrt{s} = 13$ *TeV with the ATLAS detector*, [ATLAS-CONF-2016-004](#) (2016).

[8] CMS collaboration, *Search for two Higgs bosons in final states containing two photons and two bottom quarks in proton-proton collisions at* 8 *TeV*, [*Phys. Rev.* **D 94** (2016) 052012](#) [[arXiv:1603.06896](#)] [[INSPIRE](#)].

[9] ATLAS collaboration, *Searches for Higgs boson pair production in the* $hh \to bb\tau\tau, \gamma\gamma WW^*, \gamma\gamma bb, bbbb$ *channels with the ATLAS detector*, [*Phys. Rev.* **D 92** (2015) 092004](#) [[arXiv:1509.04670](#)] [[INSPIRE](#)].

[10] ATLAS collaboration, *Search for Higgs boson pair production in the* $\gamma\gamma b\bar{b}$ *final state using pp collision data at* $\sqrt{s} = 8$ *TeV from the ATLAS detector*, [*Phys. Rev. Lett.* **114** (2015) 081802](#) [[arXiv:1406.5053](#)] [[INSPIRE](#)].

[11] ATLAS collaboration, *Search for pair production of Higgs bosons in the* $b\bar{b}b\bar{b}$ *final state using proton-proton collisions at* $\sqrt{s} = 13$ *TeV with the ATLAS detector*, [*Phys. Rev.* **D 94** (2016) 052002](#) [[arXiv:1606.04782](#)] [[INSPIRE](#)].

[12] CMS Collaboration, *Search for resonant pair production of Higgs bosons decaying to two bottom quark-antiquark pairs in proton-proton collisions at* 13 *TeV*, [CMS-PAS-HIG-16-002](#) (2016).

[13] CMS collaboration, *Search for resonant pair production of Higgs bosons decaying to two bottom quark-antiquark pairs in proton-proton collisions at* 8 *TeV*, [*Phys. Lett.* **B 749** (2015) 560](#) [[arXiv:1503.04114](#)] [[INSPIRE](#)].

[14] ATLAS collaboration, *Search for Higgs boson pair production in the $b\bar{b}b\bar{b}$ final state from pp collisions at $\sqrt{s} = 8$ TeVwith the ATLAS detector*, [*Eur. Phys. J.* **C 75** (2015) 412](#) [[arXiv:1506.00285](#)] [[INSPIRE](#)].

[15] ATLAS collaboration, *Search for Higgs boson pair production in the final state of $\gamma\gamma WW^*(\to l\nu jj)$ using $13.3\,fb^{-1}$ of pp collision data recorded at $\sqrt{s} = 13$ TeV with the ATLAS detector*, [ATLAS-CONF-2016-071](#) (2016).

[16] CMS collaboration, *Search for Higgs boson pair production in the $b\bar{b}l\nu l\nu$ final state at $\sqrt{s} = 13$ TeV*, [CMS-PAS-HIG-16-024](#) (2016).

[17] CMS collaboration, *Search for non-resonant Higgs boson pair production in the bbtautau final state using 2016 data*, [CMS-PAS-HIG-16-028](#) (2016).

[18] CMS collaboration, *Search for resonant Higgs boson pair production in the $b\bar{b}l\nu l\nu$ final state at $\sqrt{s} = 13$ TeV*, [CMS-PAS-HIG-16-011](#) (2016).

[19] CMS Collaboration, *Search for resonant Higgs boson pair production in the $b\bar{b}\tau^+\tau^-$ final state*, [CMS-PAS-HIG-16-013](#) (2016).

[20] CMS Collaboration, *Search for non-resonant Higgs boson pair production in the $b\bar{b}\tau^+\tau^-$ final state*, [CMS-PAS-HIG-16-012](#) (2016).

[21] CMS Collaboration, *Model independent search for Higgs boson pair production in the $b\bar{b}\tau^+\tau^-$ final state*, [CMS-PAS-HIG-15-013](#) (2015).

[22] M.J. Dolan, C. Englert and M. Spannowsky, *Higgs self-coupling measurements at the LHC*, [*JHEP* **10** (2012) 112](#) [[arXiv:1206.5001](#)] [[INSPIRE](#)].

[23] J. Baglio, A. Djouadi, R. Gröber, M.M. Mühlleitner, J. Quevillon and M. Spira, *The measurement of the Higgs self-coupling at the LHC: theoretical status*, [*JHEP* **04** (2013) 151](#) [[arXiv:1212.5581](#)] [[INSPIRE](#)].

[24] F. Goertz, A. Papaefstathiou, L.L. Yang and J. Zurita, *Higgs boson self-coupling measurements using ratios of cross sections*, [*JHEP* **06** (2013) 016](#) [[arXiv:1301.3492](#)] [[INSPIRE](#)].

[25] M. Gouzevitch, A. Oliveira, J. Rojo, R. Rosenfeld, G.P. Salam and V. Sanz, *Scale-invariant resonance tagging in multijet events and new physics in Higgs pair production*, [*JHEP* **07** (2013) 148](#) [[arXiv:1303.6636](#)] [[INSPIRE](#)].

[26] A.J. Barr, M.J. Dolan, C. Englert and M. Spannowsky, *Di-Higgs final states augMT2ed — Selecting hh events at the high luminosity LHC*, [*Phys. Lett.* **B 728** (2014) 308](#) [[arXiv:1309.6318](#)] [[INSPIRE](#)].

[27] M.J. Dolan, C. Englert, N. Greiner and M. Spannowsky, *Further on up the road: hhjj production at the LHC*, [*Phys. Rev. Lett.* **112** (2014) 101802](#) [[arXiv:1310.1084](#)] [[INSPIRE](#)].

[28] V. Barger, L.L. Everett, C.B. Jackson and G. Shaughnessy, *Higgs-pair production and measurement of the triscalar coupling at LHC(8,14)*, [*Phys. Lett.* **B 728** (2014) 433](#) [[arXiv:1311.2931](#)] [[INSPIRE](#)].

[29] Q. Li, Q.-S. Yan and X. Zhao, *Higgs pair production: improved description by matrix element matching*, [*Phys. Rev.* **D 89** (2014) 033015](#) [[arXiv:1312.3830](#)] [[INSPIRE](#)].

[30] P. Maierhöfer and A. Papaefstathiou, *Higgs boson pair production merged to one jet*, [*JHEP* **03** (2014) 126](#) [[arXiv:1401.0007](#)] [[INSPIRE](#)].

[31] R. Frederix et al., *Higgs pair production at the LHC with NLO and parton-shower effects*, *Phys. Lett.* **B 732** (2014) 142 [arXiv:1401.7340] [INSPIRE].

[32] D.E. Ferreira de Lima, A. Papaefstathiou and M. Spannowsky, *Standard model Higgs boson pair production in the* $(b\bar{b})(b\bar{b})$ *final state*, *JHEP* **08** (2014) 030 [arXiv:1404.7139] [INSPIRE].

[33] M. Slawinska, W. van den Wollenberg, B. van Eijk and S. Bentvelsen, *Phenomenology of the trilinear Higgs coupling at proton-proton colliders*, arXiv:1408.5010 [INSPIRE].

[34] M. Buschmann, D. Goncalves, S. Kuttimalai, M. Schonherr, F. Krauss and T. Plehn, *Mass effects in the Higgs-gluon coupling: boosted vs. off-shell production*, *JHEP* **02** (2015) 038 [arXiv:1410.5806] [INSPIRE].

[35] A. Azatov, R. Contino, G. Panico and M. Son, *Effective field theory analysis of double Higgs boson production via gluon fusion*, *Phys. Rev.* **D 92** (2015) 035001 [arXiv:1502.00539] [INSPIRE].

[36] D.A. Dicus, C. Kao and W.W. Repko, *Interference effects and the use of Higgs boson pair production to study the Higgs trilinear self coupling*, *Phys. Rev.* **D 92** (2015) 093003 [arXiv:1504.02334] [INSPIRE].

[37] A. Papaefstathiou, *Discovering Higgs boson pair production through rare final states at a* 100 *TeV collider*, *Phys. Rev.* **D 91** (2015) 113016 [arXiv:1504.04621] [INSPIRE].

[38] R. Gröber, M. Mühlleitner, M. Spira and J. Streicher, *NLO QCD corrections to Higgs pair production including dimension-6 operators*, *JHEP* **09** (2015) 092 [arXiv:1504.06577] [INSPIRE].

[39] S. Dawson, A. Ismail and I. Low, *What's in the loop? The anatomy of double Higgs production*, *Phys. Rev.* **D 91** (2015) 115008 [arXiv:1504.05596] [INSPIRE].

[40] M. Ghezzi, R. Gomez-Ambrosio, G. Passarino and S. Uccirati, *NLO Higgs effective field theory and κ-framework*, *JHEP* **07** (2015) 175 [arXiv:1505.03706] [INSPIRE].

[41] M.J. Dolan, C. Englert, N. Greiner, K. Nordstrom and M. Spannowsky, *hhjj production at the LHC*, *Eur. Phys. J.* **C 75** (2015) 387 [arXiv:1506.08008] [INSPIRE].

[42] A. Carvalho, M. Dall'Osso, T. Dorigo, F. Goertz, C.A. Gottardo and M. Tosi, *Higgs Pair Production: Choosing Benchmarks With Cluster Analysis*, *JHEP* **04** (2016) 126 [arXiv:1507.02245] [INSPIRE].

[43] S. Dawson and I.M. Lewis, *NLO corrections to double Higgs boson production in the Higgs singlet model*, *Phys. Rev.* **D 92** (2015) 094023 [arXiv:1508.05397] [INSPIRE].

[44] Q.-H. Cao, B. Yan, D.-M. Zhang and H. Zhang, *Resolving the degeneracy in single Higgs production with Higgs pair production*, *Phys. Lett.* **B 752** (2016) 285 [arXiv:1508.06512] [INSPIRE].

[45] Q.-H. Cao, Y. Liu and B. Yan, *Measuring trilinear Higgs coupling in WHH and ZHH productions at the HL-LHC*, arXiv:1511.03311 [INSPIRE].

[46] J.K. Behr, D. Bortoletto, J.A. Frost, N.P. Hartland, C. Issever and J. Rojo, *Boosting Higgs pair production in the* $b\bar{b}b\bar{b}$ *final state with multivariate techniques*, *Eur. Phys. J.* **C 76** (2016) 386 [arXiv:1512.08928] [INSPIRE].

[47] M. Gorbahn and U. Haisch, *Indirect probes of the trilinear Higgs coupling:* $gg \to h$ *and* $h \to \gamma\gamma$, arXiv:1607.03773 [INSPIRE].

[48] G. Degrassi, P.P. Giardino, F. Maltoni and D. Pagani, *Probing the Higgs self coupling via single Higgs production at the LHC*, arXiv:1607.04251 [INSPIRE].

[49] H.T. Li and J. Wang, *Fully differential Higgs pair production in association with a W boson at next-to-next-to-leading order in QCD*, arXiv:1607.06382 [INSPIRE].

[50] S. Kanemura, M. Kikuchi and K. Yagyu, *One-loop corrections to the Higgs self-couplings in the singlet extension*, arXiv:1608.01582 [INSPIRE].

[51] O.J.P. Eboli, G.C. Marques, S.F. Novaes and A.A. Natale, *Twin Higgs boson production*, *Phys. Lett.* **B 197** (1987) 269 [INSPIRE].

[52] E.W.N. Glover and J.J. van der Bij, *Higgs boson pair production via gluon fusion*, *Nucl. Phys.* **B 309** (1988) 282 [INSPIRE].

[53] T. Plehn, M. Spira and P.M. Zerwas, *Pair production of neutral Higgs particles in gluon-gluon collisions*, *Nucl. Phys.* **B 479** (1996) 46 [*Erratum ibid.* **B 531** (1998) 655] [hep-ph/9603205] [INSPIRE].

[54] S. Dawson, S. Dittmaier and M. Spira, *Neutral Higgs boson pair production at hadron colliders: QCD corrections*, *Phys. Rev.* **D 58** (1998) 115012 [hep-ph/9805244] [INSPIRE].

[55] F. Maltoni, E. Vryonidou and M. Zaro, *Top-quark mass effects in double and triple Higgs production in gluon-gluon fusion at NLO*, *JHEP* **11** (2014) 079 [arXiv:1408.6542] [INSPIRE].

[56] J. Grigo, J. Hoff, K. Melnikov and M. Steinhauser, *On the Higgs boson pair production at the LHC*, *Nucl. Phys.* **B 875** (2013) 1 [arXiv:1305.7340] [INSPIRE].

[57] J. Grigo, K. Melnikov and M. Steinhauser, *Virtual corrections to Higgs boson pair production in the large top quark mass limit*, *Nucl. Phys.* **B 888** (2014) 17 [arXiv:1408.2422] [INSPIRE].

[58] J. Grigo, J. Hoff and M. Steinhauser, *Higgs boson pair production: top quark mass effects at NLO and NNLO*, *Nucl. Phys.* **B 900** (2015) 412 [arXiv:1508.00909] [INSPIRE].

[59] G. Degrassi, P.P. Giardino and R. Gröber, *On the two-loop virtual QCD corrections to Higgs boson pair production in the Standard Model*, *Eur. Phys. J.* **C 76** (2016) 411 [arXiv:1603.00385] [INSPIRE].

[60] D. de Florian and J. Mazzitelli, *Two-loop virtual corrections to Higgs pair production*, *Phys. Lett.* **B 724** (2013) 306 [arXiv:1305.5206] [INSPIRE].

[61] D. de Florian and J. Mazzitelli, *Higgs boson pair production at next-to-next-to-leading order in QCD*, *Phys. Rev. Lett.* **111** (2013) 201801 [arXiv:1309.6594] [INSPIRE].

[62] D.Y. Shao, C.S. Li, H.T. Li and J. Wang, *Threshold resummation effects in Higgs boson pair production at the LHC*, *JHEP* **07** (2013) 169 [arXiv:1301.1245] [INSPIRE].

[63] D. de Florian and J. Mazzitelli, *Higgs pair production at next-to-next-to-leading logarithmic accuracy at the LHC*, *JHEP* **09** (2015) 053 [arXiv:1505.07122] [INSPIRE].

[64] D. de Florian et al., *Differential Higgs boson pair production at next-to-next-to-leading order in QCD*, *JHEP* **09** (2016) 151 [arXiv:1606.09519] [INSPIRE].

[65] S. Borowka et al., *Higgs boson pair production in gluon fusion at next-to-leading order with full top-quark mass dependence*, *Phys. Rev. Lett.* **117** (2016) 012001 [arXiv:1604.06447] [INSPIRE].

[66] M. Jacob and G.C. Wick, *On the general theory of collisions for particles with spin*, *Annals Phys.* **7** (1959) 404 [INSPIRE].

[67] C. Degrande et al., *Effective field theory: a modern approach to anomalous couplings*, *Annals Phys.* **335** (2013) 21 [arXiv:1205.4231] [INSPIRE].

[68] S. Dawson, E. Furlan and I. Lewis, *Unravelling an extended quark sector through multiple Higgs production?*, *Phys. Rev.* **D 87** (2013) 014007 [arXiv:1210.6663] [INSPIRE].

[69] M. Spira, *Effective multi-Higgs couplings to gluons*, *JHEP* **10** (2016) 026 [arXiv:1607.05548] [INSPIRE].

[70] G. Cullen et al., *Automated one-loop calculations with GoSam*, *Eur. Phys. J.* **C 72** (2012) 1889 [arXiv:1111.2034] [INSPIRE].

[71] G. Cullen et al., GoSam-*2.0: a tool for automated one-loop calculations within the standard model and beyond*, *Eur. Phys. J.* **C 74** (2014) 3001 [arXiv:1404.7096] [INSPIRE].

[72] P. Nogueira, *Automatic Feynman graph generation*, *J. Comput. Phys.* **105** (1993) 279 [INSPIRE].

[73] J.A.M. Vermaseren, *New features of FORM*, math-ph/0010025 [INSPIRE].

[74] J. Kuipers, T. Ueda, J.A.M. Vermaseren and J. Vollinga, *FORM version 4.0*, *Comput. Phys. Commun.* **184** (2013) 1453 [arXiv:1203.6543] [INSPIRE].

[75] A. von Manteuffel and C. Studerus, *Reduze 2 — Distributed Feynman integral reduction*, arXiv:1201.4330 [INSPIRE].

[76] A.V. Smirnov, *FIRE5: a C++ implementation of Feynman Integral REduction*, *Comput. Phys. Commun.* **189** (2015) 182 [arXiv:1408.2372] [INSPIRE].

[77] R.N. Lee, *LiteRed 1.4: a powerful tool for reduction of multiloop integrals*, *J. Phys. Conf. Ser.* **523** (2014) 012059 [arXiv:1310.1145] [INSPIRE].

[78] M. Spira, A. Djouadi, D. Graudenz and P.M. Zerwas, *Higgs boson production at the LHC*, *Nucl. Phys.* **B 453** (1995) 17 [hep-ph/9504378] [INSPIRE].

[79] R. Bonciani, P. Mastrolia and E. Remiddi, *Vertex diagrams for the QED form-factors at the two loop level*, *Nucl. Phys.* **B 661** (2003) 289 [*Erratum ibid.* **B 702** (2004) 359] [hep-ph/0301170] [INSPIRE].

[80] R. Bonciani, P. Mastrolia and E. Remiddi, *Master integrals for the two loop QCD virtual corrections to the forward backward asymmetry*, *Nucl. Phys.* **B 690** (2004) 138 [hep-ph/0311145] [INSPIRE].

[81] R. Harlander and P. Kant, *Higgs production and decay: Analytic results at next-to-leading order QCD*, *JHEP* **12** (2005) 015 [hep-ph/0509189] [INSPIRE].

[82] C. Anastasiou, S. Beerli, S. Bucherer, A. Daleo and Z. Kunszt, *Two-loop amplitudes and master integrals for the production of a Higgs boson via a massive quark and a scalar-quark loop*, *JHEP* **01** (2007) 082 [hep-ph/0611236] [INSPIRE].

[83] T. Gehrmann, S. Guns and D. Kara, *The rare decay $H \to Z\gamma$ in perturbative QCD*, *JHEP* **09** (2015) 038 [arXiv:1505.00561] [INSPIRE].

[84] R. Bonciani, V. Del Duca, H. Frellesvig, J.M. Henn, F. Moriello and V.A. Smirnov, *Next-to-leading order QCD corrections to the decay width $H \to Z\gamma$*, *JHEP* **08** (2015) 108 [arXiv:1505.00567] [INSPIRE].

[85] J. Carter and G. Heinrich, *SecDec: a general program for sector decomposition*, *Comput. Phys. Commun.* **182** (2011) 1566 [arXiv:1011.5493] [InSPIRE].

[86] S. Borowka, J. Carter and G. Heinrich, *Numerical evaluation of multi-loop integrals for arbitrary kinematics with SecDec 2.0*, *Comput. Phys. Commun.* **184** (2013) 396 [arXiv:1204.4152] [InSPIRE].

[87] S. Borowka, G. Heinrich, S.P. Jones, M. Kerner, J. Schlenk and T. Zirke, *SecDec-3.0: numerical evaluation of multi-scale integrals beyond one loop*, *Comput. Phys. Commun.* **196** (2015) 470 [arXiv:1502.06595] [InSPIRE].

[88] A. von Manteuffel, E. Panzer and R.M. Schabinger, *A quasi-finite basis for multi-loop Feynman integrals*, *JHEP* **02** (2015) 120 [arXiv:1411.7392] [InSPIRE].

[89] A. von Manteuffel, E. Panzer and R.M. Schabinger, *On the computation of form factors in massless QCD with finite master integrals*, *Phys. Rev.* **D 93** (2016) 125014 [arXiv:1510.06758] [InSPIRE].

[90] S. Dittmaier, P. Uwer and S. Weinzierl, *Hadronic top-quark pair production in association with a hard jet at next-to-leading order QCD: Phenomenological studies for the Tevatron and the LHC*, *Eur. Phys. J.* **C 59** (2009) 625 [arXiv:0810.0452] [InSPIRE].

[91] S. Catani and M.H. Seymour, *A general algorithm for calculating jet cross-sections in NLO QCD*, *Nucl. Phys.* **B 485** (1997) 291 [*Erratum ibid.* **B 510** (1998) 503] [hep-ph/9605323] [InSPIRE].

[92] D.E. Soper, *Techniques for QCD calculations by numerical integration*, *Phys. Rev.* **D 62** (2000) 014009 [hep-ph/9910292] [InSPIRE].

[93] T. Binoth, J.P. Guillet, G. Heinrich, E. Pilon and C. Schubert, *An Algebraic/numerical formalism for one-loop multi-leg amplitudes*, *JHEP* **10** (2005) 015 [hep-ph/0504267] [InSPIRE].

[94] Z. Nagy and D.E. Soper, *Numerical integration of one-loop Feynman diagrams for N-photon amplitudes*, *Phys. Rev.* **D 74** (2006) 093006 [hep-ph/0610028] [InSPIRE].

[95] Z. Li, J. Wang, Q.-S. Yan and X. Zhao, *Efficient numerical evaluation of Feynman integrals*, *Chin. Phys.* **C 40** (2016) 033103 [arXiv:1508.02512] [InSPIRE].

[96] J. Dick, F.Y. Kuo and I.H. Sloan, *High-dimensional integration: the quasi-monte carlo way*, *Acta Numerica* **22** (2013) 133.

[97] D. Nuyens and R. Cools, *Fast algorithms for component-by-component construction of rank-1 lattice rules in shift-invariant reproducing kernel Hilbert spaces*, *Math. Comput.* **75** (2006) 903.

[98] G.P. Lepage, *VEGAS: an adaptive multidimensional integration program*, CLNS-80/447 (1980).

[99] S.P. Jones, *Automation of 2-loop amplitude calculations*, PoS(LL2016)069 [arXiv:1608.03846] [InSPIRE].

[100] M. Kerner, *Next-to-leading order corrections to Higgs boson pair production in gluon fusion*, PoS(LL2016)023 [arXiv:1608.03851] [InSPIRE].

[101] Z. Nagy, *Next-to-leading order calculation of three jet observables in hadron hadron collision*, *Phys. Rev.* **D 68** (2003) 094002 [hep-ph/0307268] [InSPIRE].

[102] R. Harlander, T. Seidensticker and M. Steinhauser, *Complete corrections of order $\alpha\alpha_s$ to the decay of the Z boson into bottom quarks*, *Phys. Lett.* **B 426** (1998) 125 [hep-ph/9712228] [INSPIRE].

[103] T. Seidensticker, *Automatic application of successive asymptotic expansions of Feynman diagrams*, hep-ph/9905298 [INSPIRE].

[104] M. Steinhauser, *MATAD: a program package for the computation of MAssive TADpoles*, *Comput. Phys. Commun.* **134** (2001) 335 [hep-ph/0009029] [INSPIRE].

[105] R.V. Harlander, S. Liebler and H. Mantler, *SusHi: a program for the calculation of Higgs production in gluon fusion and bottom-quark annihilation in the Standard Model and the MSSM*, *Comput. Phys. Commun.* **184** (2013) 1605 [arXiv:1212.3249] [INSPIRE].

[106] C. Anastasiou et al., *Handbook of LHC Higgs cross sections: 4.Deciphering the nature of the Higgs sector*, LHC Higgs Cross section Working Group report (2016).

[107] J. Butterworth et al., *PDF4LHC recommendations for LHC Run II*, *J. Phys.* **G 43** (2016) 023001 [arXiv:1510.03865] [INSPIRE].

[108] S. Dulat et al., *New parton distribution functions from a global analysis of quantum chromodynamics*, *Phys. Rev.* **D 93** (2016) 033006 [arXiv:1506.07443] [INSPIRE].

[109] L.A. Harland-Lang, A.D. Martin, P. Motylinski and R.S. Thorne, *Parton distributions in the LHC era: MMHT 2014 PDFs*, *Eur. Phys. J.* **C 75** (2015) 204 [arXiv:1412.3989] [INSPIRE].

[110] NNPDF collaboration, R.D. Ball et al., *Parton distributions for the LHC Run II*, *JHEP* **04** (2015) 040 [arXiv:1410.8849] [INSPIRE].

[111] F. Caola, S. Forte, S. Marzani, C. Muselli and G. Vita, *The Higgs transverse momentum spectrum with finite quark masses beyond leading order*, *JHEP* **08** (2016) 150 [arXiv:1606.04100] [INSPIRE].

[112] N. Greiner, S. Hoeche, G. Luisoni, M. Schonherr and J.-C. Winter, *Full mass dependence in Higgs boson production in association with jets at the LHC and FCC*, arXiv:1608.01195 [INSPIRE].

[113] M.L. Mangano et al., *Physics at a 100 TeV pp collider: standard model processes*, arXiv:1607.01831 [INSPIRE].